

## Design of single-phased magnesium alloys with typically high solubility rare earth elements for biomedical applications: Concept and proof

Dong Bian<sup>a,1</sup>, Xiao Chu<sup>a,1</sup>, Jin Xiao<sup>b,1</sup>, Zhipei Tong<sup>b,1</sup>, He Huang<sup>c</sup>, Qinggong Jia<sup>c</sup>, Jianing Liu<sup>d</sup>, Wenting Li<sup>e</sup>, Hui Yu<sup>b</sup>, Yue He<sup>b</sup>, Limin Ma<sup>a</sup>, Xiaolan Wang<sup>a</sup>, Mei Li<sup>a</sup>, Tao Yang<sup>b</sup>, Wenhan Huang<sup>b</sup>, Chi Zhang<sup>b</sup>, Mengyu Yao<sup>b</sup>, Yu Zhang<sup>b,\*\*\*\*</sup>, Zhigang Xu<sup>f,\*\*\*</sup>, Shaokang Guan<sup>c,\*\*</sup>, Yufeng Zheng<sup>b,e,\*</sup>

<sup>a</sup> Medical Research Center, Guangdong Provincial People's Hospital, Guangdong Academy of Medical Sciences, Guangzhou, 510080, China

<sup>b</sup> Department of Orthopedics, Guangdong Provincial People's Hospital, Guangdong Academy of Medical Sciences, Guangzhou, 510080, China

<sup>c</sup> School of Materials Science and Engineering, Zhengzhou University, Zhengzhou, 450001, China

<sup>d</sup> Academy for Advanced Interdisciplinary Studies, Peking University, Beijing, 100871, China

<sup>e</sup> School of Materials Science and Engineering, Peking University, Beijing, 100871, China

<sup>f</sup> ERC for Revolutionizing Metallic Biomaterials, North Carolina A&T State University, Greensboro, NC, 27411, USA

### ARTICLE INFO

#### Keywords:

Biodegradable magnesium  
Rare earth  
Bimodal grain structure  
Mechanical property  
Corrosion resistance

### ABSTRACT

Rare earth elements (REEs) have been long applied in magnesium alloys, among which the mischmetal-containing WE43 alloy has already got the CE mark approval for clinical application. A considerable amount of REEs (7 wt%) is needed in that multi-phased alloy to achieve a good combination of mechanical strength and corrosion resistance. However, the high complex RE addition accompanied with multiple second phases may bring the concern of biological hazards. Single-phased Mg-RE alloys with simpler compositions were proposed to improve the overall performance, i.e., "Simpler alloy, better performance". The single-phased microstructure can be successfully obtained with typical high-solubility REEs (Ho, Er or Lu) through traditional smelting, casting and extrusion in a wide compositional range. A good corrosion resistance with a macroscopically uniform corrosion mode was guaranteed by the homogeneously single-phased microstructure. The bimodal-grained structure with plenty of sub-grain microstructures allow us to minimize the RE addition to <1 wt%, without losing mechanical properties. The single-phased Mg-RE alloys show comparable mechanical properties to the clinically-proven Mg-based implants. They exhibited similar *in-vitro* and *in-vivo* performances (without local or systematic toxicity in SD-rats) compared to a high purity magnesium. In addition, metal elements in our single-phased alloys can be gradually excreted through the urinary system and digestive system, showing no consistent accumulation of RE in main organs, i.e., less burden on organs. The novel concept in this study focuses on the simplification of Mg-RE based alloys for biomedical purpose, and other biodegradable metals with single-phased microstructures are expected to be explored.

### 1. Introduction

It has a profound history to use rare earth elements (REEs) as a

metallurgical addition in magnesium (Mg) to adjust or improve the castability, workability, mechanical properties, corrosion resistance, and some other properties [1–3]. During the last 20 years, Mg-RE based

Peer review under responsibility of KeAi Communications Co., Ltd.

\* Corresponding authors. Department of Orthopedics, Guangdong Provincial People's Hospital, Guangdong Academy of Medical Sciences, Guangzhou, 510080, China.

\*\* Corresponding author.

\*\*\* Co-corresponding author.

\*\*\*\* Co-corresponding author.

E-mail addresses: [luck\\_2001@126.com](mailto:luck_2001@126.com) (Y. Zhang), [zhigang@ncat.edu](mailto:zhigang@ncat.edu) (Z. Xu), [skguan@zzu.edu.cn](mailto:skguan@zzu.edu.cn) (S. Guan), [yfzheng@pku.edu.cn](mailto:yfzheng@pku.edu.cn) (Y. Zheng).

<sup>1</sup> Those authors contributed equally to this work.

<https://doi.org/10.1016/j.bioactmat.2022.09.018>

Received 5 August 2022; Received in revised form 15 September 2022; Accepted 16 September 2022

2452-199X/© 2022 The Authors. Publishing services by Elsevier B.V. on behalf of KeAi Communications Co. Ltd. This is an open access article under the CC BY-NC-ND license (<http://creativecommons.org/licenses/by-nc-nd/4.0/>).

alloys have been extensively explored to be used as biodegradable metals for biomedical applications, owing to their superior mechanical properties and corrosion resistance [4,5]. The first two clinically-proven Mg-based implants, one for orthopedic screw (MAGNEZIX®, Syntellix AG, Germany) and the other for cardiovascular stent (Magmaris®, BIOTRONIK, Germany), are all based on RE containing alloys, i.e., the WE43 modified ones [6–8].

The term REEs, as defined by the International Union of Pure and Applied Chemistry, applies to 17 elements, including scandium (Sc), yttrium (Y), and the lanthanide series of 15 elements [9]. Basic properties, including atomic radius, crystal structure, solid-solubility, etc., of all the RE elements are listed in Table 1 for comparison [10–12]. Generally, REEs can be roughly classified into two categories considering their solubilities in Mg, i.e., the high-solubility group including Y, Gd, Tb, Dy, Ho, Er, Tm, Yb and Lu, and the low/limited-solubility group including La, Ce, Pr, Nd, Sm and Eu. RE elements with high solubility can be entirely dissolved into the Mg matrix in a wide composition range, so as to get a uniformly single-phased microstructure.

Some unique properties could be possibly obtained in Mg-RE alloys with single-phased microstructures. On the one hand, the corrosion behavior of single-phased Mg-RE alloys is worth expecting. Galvanic corrosion between the  $\alpha$ -Mg matrix and the second phases could be basically avoided in single-phased alloys [13,14]. Dissolved REEs in the crystal lattice might improve the corrosion potential of the alloy matrix, and stabilize the matrix from the thermodynamic aspect. In addition, effects of dissolved REEs on the formation and stability of the degradation product layer are interesting to explore [15,16]. A good corrosion resistance with a uniform corrosion mode is hopefully expected. On the other hand, mechanical properties of single-phased Mg-RE alloys can be substantially improved compared to those of pure Mg, owing to the grain refinement strengthening and solid solution strengthening effects of dissolved REEs [3,17]. Apart from the above two aspects, the puzzle whether the second phases can be corroded/degraded, and how those second phases can be metabolized in multi-phased Mg alloys should no longer be a concern in single-phased Mg-RE alloys. Thus, single-phased Mg-RE alloys seem to be suitable for biomedical applications.

Among the high-solubility REEs, the maximum solubility of Ho, Er, Tm or Lu in Mg is extremely high (>28 wt%) [10]. They can be added into Mg to form single-phased alloys in a wide concentration range by

traditional smelting and casting, even without extra solid solution treatment. Ho is a moderately hard, silvery white metal that is relatively stable in air. It owns a hexagonal close-packed structure with similar atomic radius and standard electrode potential compared to those of Mg (Table 1). Ho has been used as a component of some electronic and optical devices, and it has been explored to be used in biomedical applications [18]. In the present study, Holmium (Ho) was chosen as a typical high-solubility RE to obtain a series of single-phased alloys, since Ho is convenient to get at a relatively low price. The highest Ho content was set at 7 wt%, which was equivalent to the total RE contents in WE43 alloy according to DIN EN 1753 [19]. Minor Zirconium (Zr) as an effective grain-refinement element was also added to further refine the grains, and to improve microstructural homogeneity [20,21]. The total amount of Zr was limited to <0.4 wt% (similar to the Zr content in WE43), and no extra phases would be generated at this concentration during a rapid cooling process. This Zr concentration was normally found in biodegradable Mg alloys, and would not induce local or systematic toxicity [22–24].

The single-phased microstructures of as-obtained Mg–Ho based alloys were examined via metallographic observation, electron back-scattered diffraction (EBSD), X-ray diffraction (XRD), and transmission electron microscopy (TEM). Mechanical properties, *in-vitro* degradation behaviors and *in-vitro* biocompatibility of those alloys were generally investigated, and compared with a high purity Mg (denoted as HP-Mg, the most typical  $\alpha$ -Mg single-phased microstructure with an excellent corrosion resistance and a uniform corrosion mode). Based on the *in-vitro* results, one typical single-phased alloy was chosen and implanted into rat femoral condyle, with a HP-Mg implant as control. *In-vivo* degradation behaviors, local tissue responses, potential local and systemic toxicities were systematically evaluated by performing micro-CT scanning, histopathological observation and overall biochemical analysis. The time-relevant distribution & concentration of metal elements in different tissues, body fluids and excreta were characterized, to reveal the possible metabolic pathways of Mg implant. The concept and feasibility of developing single-phased biodegradable metals with high solubility REEs were comprehensively discussed, pursuing the goal of “simpler alloy, better performance”. In the end, future work on this topic was also proposed.

**Table 1**  
Basic physicochemical properties of REEs [10,11].

| Atomic No. | Element      | Symbol | Density (g/cm <sup>3</sup> ) | Melting/boiling point (°C) | Crystal structure (RT) <sup>a</sup> | Atomic radius (nm) | Maximum solubility in Mg (wt.%) | Standard electrode potential (V) <sup>b</sup> | Phase diagram type (Mg-rich corner) |
|------------|--------------|--------|------------------------------|----------------------------|-------------------------------------|--------------------|---------------------------------|---|-------------------------------------|
| 21         | Scandium     | Sc     | 2.985                        | 1541/2830                  | HCP                                 | 0.1620             | ~24.5                           | −2.077  | Peritectic                          |
| 39         | Yttrium      | Y      | 4.472                        | 1526/3336                  | HCP                                 | 0.1800             | 12.4                            | −2.372  | Eutectic                            |
| 57         | Lanthanum    | La     | 6.146                        | 920/3470                   | Hexagonal                           | 0.1620             | 0.23                            | −2.379  | Eutectic                            |
| 58         | Cerium       | Ce     | 6.689                        | 795/3360                   | FCC                                 | 0.1818             | 0.74                            | −2.336  | Eutectic                            |
| 59         | Praseodymium | Pr     | 6.640                        | 935/3290                   | Hexagonal                           | 0.1824             | ~0.6                            | −2.353  | Eutectic                            |
| 60         | Neodymium    | Nd     | 6.800                        | 1024/3100                  | Hexagonal                           | 0.1814             | 3.6                             | −2.323  | Eutectic                            |
| 61         | Promethium   | Pm     | 7.264                        | 1100/3000                  | BCC                                 | 0.185              | 4.5 (proposed) <sup>c</sup>     | −2.30   | Eutectic                            |
| 62         | Samarium     | Sm     | 7.353                        | 1072/1803                  | Rhombohedral                        | 0.1804             | ~6.4                            | −2.304  | Eutectic                            |
| 63         | Europium     | Eu     | 5.244                        | 826/1527                   | BCC                                 | 0.2084             | 0                               | −1.991  | Eutectic                            |
| 64         | Gadolinium   | Gd     | 7.901                        | 1312/3250                  | HCP                                 | 0.1804             | 23.49                           | −2.279  | Eutectic                            |
| 65         | Terbium      | Tb     | 8.219                        | 1356/3230                  | HCP                                 | 0.1773             | 24.0                            | −2.28   | Eutectic                            |
| 66         | Dysprosium   | Dy     | 8.551                        | 1407/2567                  | HCP                                 | 0.1781             | 25.8                            | −2.295  | Eutectic                            |
| 67         | Holmium      | Ho     | 8.795                        | 1461/2720                  | HCP                                 | 0.1762             | 28.08                           | −2.33   | Eutectic                            |
| 68         | Erbium       | Er     | 9.066                        | 1529/2868                  | HCP                                 | 0.1761             | 33.8                            | −2.331  | Eutectic                            |
| 69         | Thulium      | Tm     | 9.321                        | 1545/1950                  | HCP                                 | 0.1759             | 31.8                            | −2.319  | Eutectic                            |
| 70         | Ytterbium    | Yb     | 6.570                        | 824/1196                   | FCC                                 | 0.1933             | 8.0                             | −2.19   | Eutectic                            |
| 71         | Lutetium     | Lu     | 9.841                        | 1652/3402                  | HCP                                 | 0.1738             | ~41                             | −2.28   | Eutectic                            |

<sup>a</sup> HCP: hexagonal close-packed structure, FCC: face-centered cubic structure, BCC: body-centered cubic structure.

<sup>b</sup> Reaction:  $RE^{3+} + 3e \rightleftharpoons RE$ , referred to standard hydrogen electrode.

<sup>c</sup> There is no experimental study on the Mg–Pm phase diagram. The current existing Mg–Pm binary phase diagram was assumed. Different from other REs, Pm is radioactive.

## 2. Materials and methods

### 2.1. Materials

Alloys were prepared by using a commercial pure Mg (99.97 wt%), a Mg-30Ho master alloy and a Mg-30Zr master alloy in the laboratory of ERC for Revolutionizing Metallic Biomaterials (North Carolina A&T State University). The melt was stirred for 20 min in a resistance furnace with Ar gas as protective atmosphere before pouring into a graphite mold, which has been preheated at 300 °C. The cast ingots were directly extruded at 350 °C with an extrusion ratio of 15 to obtain the finished 12 mm-diameter rods. The single-phased alloys were denoted as SPMg-xHo with different Ho content hereinafter. The raw pure magnesium (Mg, 99.97 wt%) and a high purity magnesium (HP-Mg, 99.99 wt%) were adopted as control materials. The nominal and actual compositions of the experimental materials were listed in Table 2.

Specimens for microstructural characterization, corrosion test and *in-vitro* biological evaluation were cut into  $\Phi 12$  mm  $\times$  1 mm disks (as-extruded rod) and 10 mm  $\times$  10 mm  $\times$  1 mm square pieces (as-cast ingot). Tensile specimens were machined according to ASTM E8/E8M-16a [25]. Samples for compression test were machined into  $\Phi$  3.5 mm  $\times$  7 mm cylinders parallel to the extrusion direction, according to ASTM E9-19 [26]. Cylindrical pins ( $\Phi 1.0$  mm  $\times$  6.5 mm) were cut along the extrusion direction for *in-vivo* experiment. All the samples were mechanically polished up to 2000 grit with SiC sandpapers, and then ultrasonically cleaned in acetone and absolute ethanol, respectively. Samples for cell assays were sterilized under ultraviolet radiation for 2 h of each side. Cylindrical pins for animal test were separately encapsulated and sterilized under Co60  $\gamma$  ray radiation at 25 kGy.

### 2.2. Microstructural characterization

Specimens for microstructural observation were further polished into a mirror-like surface with 5  $\mu$ m diamond polishing paste. After being cleaned in absolute ethanol, the polished samples were etched in 4% HNO<sub>3</sub>/ethanol or 4% HNO<sub>3</sub>/H<sub>2</sub>O solution. An optical microscope (Olympus BX51M, Japan) was employed to observe the microstructure. The average grain size was calculated in ImageJ software (ImageJ 1.43 u, USA) through a linear intercept method according to ASTM E112-13 [27]. EBSD test was performed to dissect more microstructural details. Samples were further polished on an argon (Ar) ion milling system (IM4000 Plus, Hitachi, Japan), and they were observed under a scanning electron microscope (Gemini SEM 300, ZEISS, Germany) equipped with an Oxford C-nano detector. EBSD data were processed with Channel 5 software (HKL Technology, USA). An X-ray diffractometer (XRD, Rigaku DMAX 2400, Japan) was employed to identify the constituent phases, by using Cu K $\alpha$  radiation at a scan rate of 2°/min operated at 40 kV and 100 mA. For TEM analysis, samples were first treated with mechanical thinning, then followed by ion milling (GATAN 691, USA). High-resolution transmission electron microscopy (HR-TEM) images and selected area electron diffraction (SAED) were acquired on a scanning transmission electron microscope (Talos F200X, Thermo Fisher Scientific, USA).

**Table 2**  
Chemical compositions of the experimental materials.

| Sample     | Chemical compositions (wt.%) |      |        |         |         |         |        |        |        |      |
|------------|------------------------------|------|--------|---------|---------|---------|--------|--------|--------|------|
|            | Ho                           | Zr   | Fe     | Cu      | Ni      | Co      | Si     | Mn     | Al     | Mg   |
| Mg         | /                            | /    | 0.0012 | 0.00087 | 0.00089 | 0.00058 | 0.0026 | 0.0028 | 0.0037 | Bal. |
| HP-Mg      | /                            | /    | 0.0010 | 0.00040 | 0.00030 | 0.00020 | 0.0020 | 0.0011 | 0.0002 | Bal. |
| SPMg-0.5Ho | 0.52                         | 0.38 | 0.0012 | 0.00051 | 0.00072 | 0.00043 | 0.0025 | 0.0021 | 0.0031 | Bal. |
| SPMg-1.0Ho | 0.92                         | 0.42 | 0.0013 | 0.00054 | 0.00075 | 0.00044 | 0.0027 | 0.0022 | 0.0033 | Bal. |
| SPMg-3.0Ho | 2.51                         | 0.41 | 0.0014 | 0.00055 | 0.00076 | 0.00046 | 0.0028 | 0.0023 | 0.0032 | Bal. |
| SPMg-5.0Ho | 4.58                         | 0.39 | 0.0012 | 0.00057 | 0.00080 | 0.00050 | 0.0026 | 0.0025 | 0.0033 | Bal. |
| SPMg-7.0Ho | 6.65                         | 0.26 | 0.0013 | 0.00061 | 0.00081 | 0.00051 | 0.0030 | 0.0025 | 0.0034 | Bal. |

### 2.3. Mechanical behaviors

Mechanical tests were performed on a universal testing machine (Instron 5969, USA) at room temperature (25 °C). An extensometer was used during tensile test, and the strain rate was set at  $5 \times 10^{-4}$  s<sup>-1</sup>. Tensile mechanical parameters including elastic modulus (E), tensile yield strength (TYS), ultimate tensile strength (UTS), and elongation (El.) can be derived from the tensile stress-strain curves. During compressive test, the compressive crosshead speed was 1 mm/min. Parameters including compressive yield strength (CYS), ultimate compressive strength (UCS), uniform strain (US) and total compressive strain (CS) before failure can be acquired from the compressive stress-strain curves. Five parallel specimens were adopted for each material.

### 2.4. In-vitro degradation behaviors

#### 2.4.1. Electrochemical test

Electrochemical test was carried out in a traditional three-electrode cell system by using a platinum foil as counter electrode (CE), a saturated calomel electrode (SCE) as reference electrode, and the test sample with an exposed area of 0.45 cm<sup>2</sup> as working electrode. The test was performed in Hank's solution on an electrochemical workstation (PGSTAT 302N, Metrohm Autolab, Switzerland). Chemical compositions and preparation procedures of Hank's solution can be found elsewhere [28]. Open circuit potential (OCP) was continuously monitored for 3600 s, then electrochemical impedance spectroscopy (EIS) was measured. The potentiodynamic polarization (PDP) test was performed at a scanning rate of 1 mV/s. Electrochemical corrosion parameters, including corrosion potential ( $E_{corr}$ ) and corrosion current density ( $i_{corr}$ ), were estimated from the polarization curves by means of Tafel analysis, according to ASTM-G102-89 [29]. Five duplicate samples were measured for each material.

#### 2.4.2. Immersion test

The immersion test was carried out to observe the long-term corrosion behaviors without external interferences. Samples were immersed in Hank's solution at  $37 \pm 0.5$  °C with an exposure ratio of 20 mL/cm<sup>2</sup>, according to ASTM F3268-18a and ASTM G31-72 [30,31]. The pH value during immersion was daily recorded. After immersion for 3 and 15 days, samples were taken out of the solution, gently rinsed with distilled water, and dried in open air, respectively. Surface morphology was recorded both under a digital camera (EOS 70D, Canon, Japan) and under a scanning electron microscope (SEM, Hitachi S-4800, Japan). Surface chemical compositions were characterized by using energy dispersive spectroscopy (EDS) under SEM and through an imaging X-ray photoelectron spectrometer (XPS, Axis Ultra, Kratos Analytical Ltd., UK) with Al K $\alpha$  radiation. High resolution narrow scanning was performed to determine the binding states of existing elements. Fourier transform infrared spectroscopy (FTIR, Nicolet iS 50, Thermo Scientific, USA) was utilized to identify the functional groups in the degradation products in the range of 4000 to 500 cm<sup>-1</sup>. Crystalline phases in the degradation products were identified by XRD. Cross-sectional morphology was also observed under SEM. The elemental distribution in the degradation

product layer was scanned by performing EDS mapping analysis.

Sample weight loss was also measured after removing the degradation products in chromic acid, according to ASTM G1-03 [32]. Corrosion rate was calculated by using the following equation,  $v_{corr} = 3.65\Delta W/\rho$ ; where  $\Delta W$  is the metal weight loss rate ( $\text{mg}/\text{cm}^2/\text{d}$ ), and  $\rho$  is the metal density ( $\text{g}/\text{cm}^3$ ) [33]. A total of six parallel samples were employed for each material, among which one sample was used for cross-section analysis, and the remaining samples were used for corrosion surface analysis, afterwards, they were cleaned in chromic acid for weight loss measurement.

## 2.5. In-vitro biocompatibility

### 2.5.1. Preparation of alloy extracts

The alloy extracts were prepared by soaking the sample in minimum essential medium alpha ( $\alpha$ -MEM, Gibco, Thermo Fisher, USA) supplemented with 10% fetal bovine serum (FBS, Gibco, Thermo Fisher, USA), with an extraction ratio of  $1.25 \text{ cm}^2/\text{mL}$  in a humidified atmosphere supplied with 5%  $\text{CO}_2$  at  $37^\circ\text{C}$  for 24 h. The supernatant was withdrawn and stored at  $4^\circ\text{C}$  before use. The extract was discarded if the storage time exceeded 5 days.

### 2.5.2. Cell cytotoxicity

Cytotoxicity of the experimental materials was evaluated through indirect cell assay, according to ISO 10993-5:2009(E) [34]. Murine pre-osteoblast cells MC3T3-E1 (ATCC, CRL-12424) were cultured in  $\alpha$ -MEM medium containing 10% FBS at  $37^\circ\text{C}$  in a humidified atmosphere supplied with 5%  $\text{CO}_2$ . Cells were seeded onto 96-well culture plates at a density of  $2 \times 10^4 \text{ ml}^{-1}$  ( $100 \mu\text{l}$  in each well). After incubation for 24 h to allow attachment, the medium was replaced by different alloy extracts. Normal cell culture medium ( $\alpha$ -MEM+10% FBS) was set as blank control. The extracts/medium were refreshed every 3 days. After incubation for 1, 3 and 5 days, cells were gently rinsed with phosphate-buffered saline (PBS) for 3 times. Afterwards,  $10 \mu\text{L}$  Cell Counting Kit-8 (CCK-8, DOJINDO, Japan) solution was added, and cells were further incubated for another 4 h. The spectrophotometric absorbance of each well was measured at  $450 \text{ nm}$  by using a microplate reader (Bio-Rad 680, USA). Each experiment was carried out with 5 parallel wells.

LIVE/DEAD cell assay was also performed according to the manufacturer's protocol (LIVE/DEAD staining kit, BestBio, China). Cells were cultured according to the protocols as described in the CCK-8 assay. LIVE/DEAD staining reagent ( $100 \mu\text{L}$ ) was added after the cells were gently rinsed with PBS solution. After incubation for 30 min at  $37^\circ\text{C}$  in darkness, the remaining dye was removed. Then,  $100 \mu\text{L}$  of normal culture medium was added after the cells were gently washed with PBS. Live and dead cells were then captured under a fluorescence microscope (Leica DMI4000B, Germany).

### 2.5.3. Alkaline phosphatase (ALP) activity

MC3T3-E1 cells were seeded at a density of  $1 \times 10^4$  cells per well in 24-well plates. After incubation for 24 h, the culture medium was replaced by alloy extracts added with  $0.01 \mu\text{M}$  dexamethasone,  $10 \text{ mM}$  sodium- $\beta$ -glycerophosphate and  $50 \mu\text{g}/\text{mL}$  ascorbic acid (Sigma, USA). The extracts/medium were refreshed every 2 days. After 7 and 14 days of culture, the medium was removed, and cells were lysed. The intracellular ALP activities were measured by using the Alkaline Phosphatase Assay Kit (Beyotime Biotechnology, China). Three duplicate samples were measured for each material.

### 2.5.4. Osteogenesis-related gene expression

MC3T3-E1 cells were cultured in different alloy extracts supplemented with  $0.01 \mu\text{M}$  dexamethasone,  $10 \text{ mM}$  sodium- $\beta$ -glycerophosphate and  $50 \mu\text{g}/\text{mL}$  ascorbic acid for 14 days. Then, total RNA was isolated using the Trizol reagent (Thermo Fisher, USA). The RNA concentrations were quantified with the Nanodrop 2000 UV-Vis

Spectrophotometer (Thermo Fisher, USA). Quantitative real time-polymerase chain reaction (qRT-PCR) was carried out using  $1 \mu\text{g}$  of total RNA, which was reversely transcribed into complementary DNA using the Reverse Transcription Kit (Takara, Japan), according to the user guide. The qRT-PCR was performed by using the SYBR Green RT-PCR Kit (Takara, Japan), and the qRT-PCR assays were performed on Rotor gene Q (Qiagen, Germany). All reactions were carried out in triplicate and the qRT-PCR results were analyzed by using the Rotor-Gene Real-Time analysis software 6.0. Then, relative gene expression was calculated using the  $2^{-\Delta\Delta\text{Ct}}$  method. The primer sequences of osteogenesis-related genes were listed in Table S1.

## 2.6. In-vivo animal trial

### 2.6.1. Animal model and surgery

Thirty male Sprague Dawley rats (SD-rat, SPF level) weighing 200–250 g were provided by the Laboratory Animal Center of Guangzhou General Hospital of Guangzhou Military Command of PLA. Animals were randomly and evenly divided into two groups. One group received implantation of the experimental single-phased alloy, and the other group received HP-Mg implantation. Animals were anaesthetized by intraperitoneal injection of pentobarbital sodium at a dosage of  $40 \text{ mg}/\text{kg}$ . Operation sites around the knee joint were shaved and sterilized, followed by decortication. A hole ( $1 \text{ mm}$ ) was drilled through the femoral condyle by using an orthopedic electro-drill after exposure of the joint. Then, a  $\Phi 1.0 \text{ mm} \times 6.5 \text{ mm}$  pin was inserted into the hole. The implantation was performed on both legs. After surgery, animals were kept in separated cages with free access to food and clean drinking water. Five animals in each group were sacrificed at 1, 3 and 7 m post-operation, respectively. The surgical procedures and postoperative care protocols were fulfilled the requirements of the Ethics Committee of Guangdong Provincial People's Hospital (Animal Trial Permit No. KY-D-2021-175-02).

### 2.6.2. Postoperative observation

All animals were clinically examined for general conditions and in particular for significant signs of lameness, infection, subcutaneous emphysema formation and loss of appetite. Any difference between the two groups should be carefully noted.

### 2.6.3. Blood analysis

At the scheduled time for sacrifice, animals were deep anaesthetized by using overdosed pentobarbital sodium, and animal blood was collected from the abdominal aorta. Blood samples ( $1 \text{ mL}$ ) for routine examination (XT-2000iv, Sysmex Corporation, Japan) were anticoagulated with EDTAK2. The  $5 \text{ mL}$  blood without any anticoagulant additions was used for blood biochemistry analysis (Hitachi 7100, Japan). Blood samples ( $2 \text{ mL}$ ) anticoagulated with heparin sodium were used for coagulation analysis (Sysmex CA510, Japan). All the blood analysis was performed in Guangzhou General Pharmaceutical Research Institute Co.,Ltd.

### 2.6.4. Micro-CT analysis

Rat femurs were retrieved and scanned under a micro-CT scanner (LaTheta LCT-200, Japan) with a spatial resolution of  $48 \mu\text{m}$ . High resolution scanning was performed on a Skyscan1172 (Bruker, Belgium) micro-CT scanner with a spatial resolution of  $20 \mu\text{m}$  ( $n = 5$ ). The bone mineral density (BMD) and bone volume/tissue volume ratio (BV/TV) around the implant ( $\sim 1 \text{ mm}$  range) were calculated. Three-dimensional (3D) reconstruction and two-dimensional (2D) slices were performed in Amira software (Amira 6.0.1, Visage Imaging). The remaining implant was reconstructed, and volume of the implant was quantified.

### 2.6.5. Histopathological analysis

Retrieved rat femurs and main organs (heart, liver, spleen, lung, kidney, pancreas, intestine, brain and muscle adjacent to the

implantation site) were fixed in 4% paraformaldehyde/PBS solution (Servicebio, China). Rat femurs were decalcified with ethylene diamine tetraacetic acid solution (EDTA, 0.5 M, Servicebio, China). Soft tissues and decalcified bones were dehydrated in gradient ethanol/distilled water mixtures, embedded in paraffin, cut into 4 μm sections, and stained with hematoxylin-eosin dye (H&E, Servicebio, China) sequentially. Histological observation was performed under an inverted

microscope (Olympus IX73, Japan).

### 2.6.6. Metal element analysis

Inductively coupled plasma mass spectrometry (ICP-MS, DRC-II, PerkinElmer, USA) and inductively coupled plasma optical emission spectrometry (ICP-OES, iCAP 6000, Thermo, England) were employed for element analysis. Blood serum after the blood biochemical test was

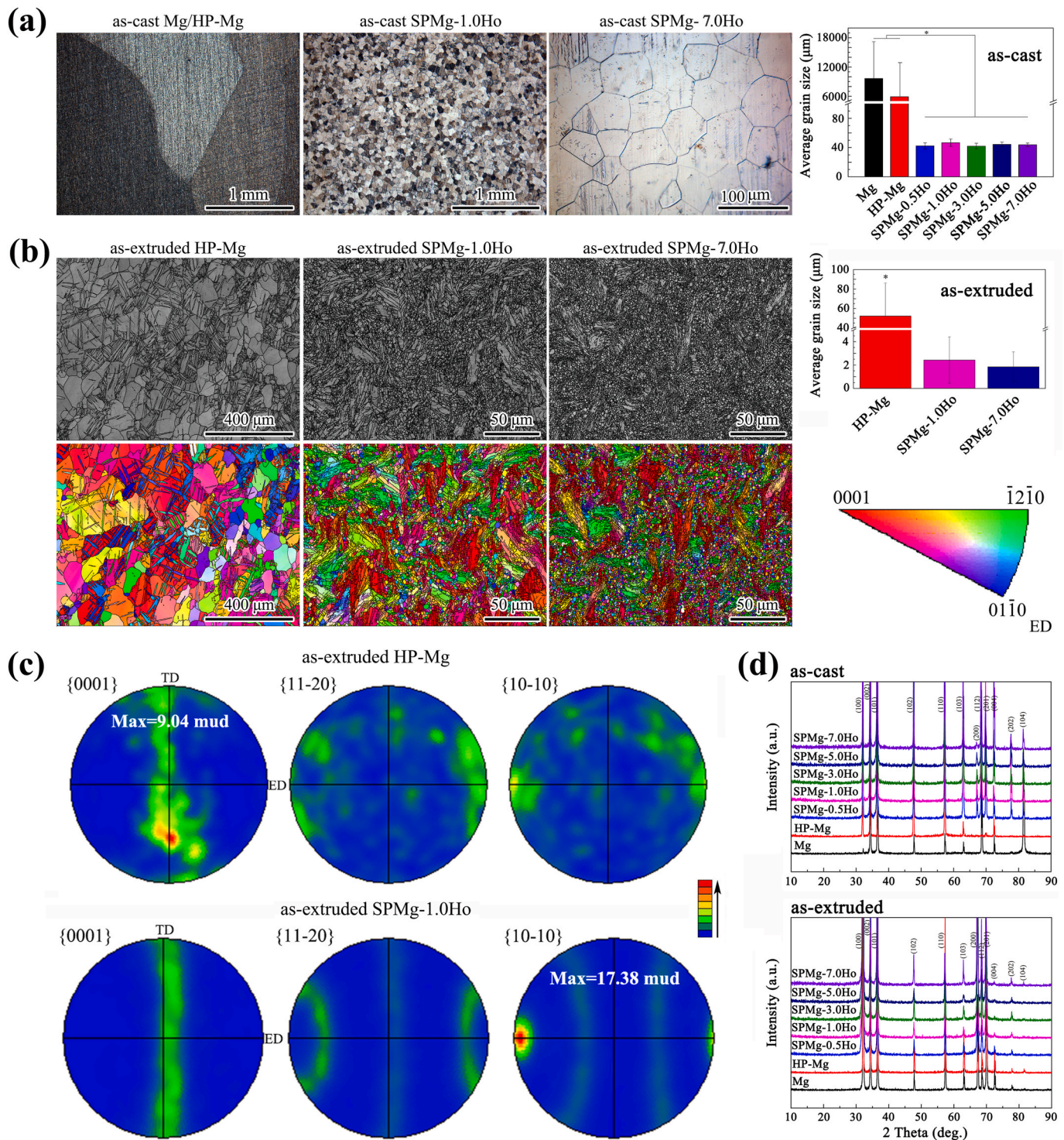


**Fig. 1.** (a) Optical microstructures of as-cast Mg/HP-Mg and two typical SPMg-xHo alloys (x = 1.0, 7.0) in as-cast condition; (b) band contrast (BC) maps and corresponding inverse polar figure (IPF) maps of two typical SPMg-xHo alloys in as-extruded condition compared to those of as-extruded HP-Mg, average grain sizes of the alloys were also listed; (c) Pole figures corresponding to {0001}, {11-20} and {10-10} planes of as-extruded HP-Mg and SPMg-1.0Ho; (d) XRD patterns of the experimental materials both in as-cast condition and in as-extruded condition.

used for element analysis. Main organs were retrieved for element analysis. Fresh organs were carefully dissociated, and any adipose tissues or connective tissues were stripped. Then, 200 mg tissues were weighed and smashed before use. Animal urine and feces were also collected for element analysis. Animal feces were dried and grinded, then 500 mg was used for the analysis. All the biological samples were digested in nitric acid (GR level) with the assistance of microwave, and proper diluted before test.

2.7. Statistical analysis

Quantitative results are expressed as mean ± standard deviation. Statistical differences were analyzed by using the analysis of variance (ANOVA) followed by Tukey test, and a *p*-value < 0.05 was considered as statistically significant. Symbol \* means significant difference at the 0.01 level, meanwhile, symbol • means significant difference at the 0.05 level.

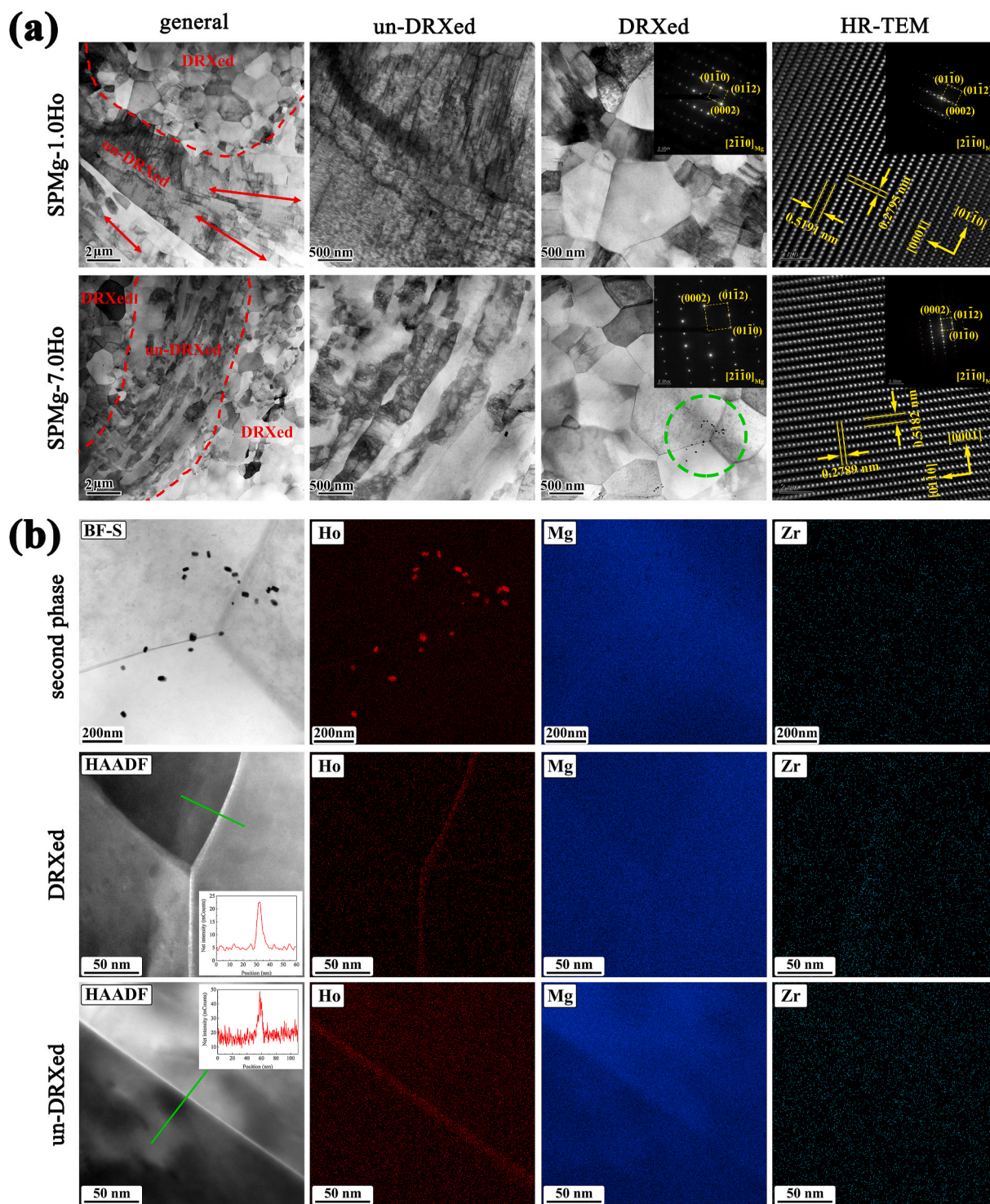


Fig. 2. (a) Microstructural details of two as-extruded SPMg-xHo alloys (x = 1.0, 7.0) showing typical bimodal graded structures with corresponding SAED patterns and HR-TEM atomic arrangements. Red arrows indicate the elongated direction of the un-DRXed regions; (b) HR-EDS mapping analysis at typical sites, including second phases (green circle in Fig. 2 (a)), typical grain boundaries at DRXed and un-DRXed regions.

### 3. Results

#### 3.1. The single-phased microstructure

Fig. 1 displays the typical microstructures of SPMg-xHo series alloys and their corresponding XRD patterns. As-cast Mg and as-cast HP-Mg owned a similar microstructure with a little difference in grain size. Microstructures of the SPMg-xHo series alloys were similar, so only SPMg-1.0Ho and SPMg-7.0Ho were displayed. The as-cast SPMg-xHo series alloys exhibited uniform microstructures with equiaxed grains, and no second phases were found. There was no significant difference in the grain size among different SPMg-xHo alloys. The average grain size of SPMg-xHo alloys ( $<50 \mu\text{m}$ ) was significantly smaller than that of Mg or HP-Mg (both  $>5 \text{mm}$  in as-cast condition).

After extrusion, the microstructures were substantially refined. The average grain size of as-extruded HP-Mg was reduced to  $52.3 \pm 33.8 \mu\text{m}$ , and plenty of twins existed (Fig. 1 (b) and Fig. S1 (b)). As-extruded SPMg-xHo alloys exhibited fine-grained microstructures with an average grain size of less than  $2.5 \mu\text{m}$ , and they were composed of dynamically recrystallized (DRXed) zones (fine and equiaxed grains) and un-dynamically recrystallized (un-DRXed) zones (twisted and elongated grains), showing the typical morphology of a bimodal grain structure. Within the un-DRXed zones, the coarser grains were prone to own similar crystal orientations. However, within the DRXed zones, the fine equiaxed grains owned random orientations (Fig. 1 (b)). The average grain sizes of SPMg-1.0Ho and SPMg-7.0Ho were  $2.4 \pm 1.9 \mu\text{m}$  and  $1.8 \pm 1.3 \mu\text{m}$ , respectively. Abundant sub-grain microstructures (not twins) and deformed zones were found in the as-extruded SPMg-xHo alloys, and no extra second phase was detected through EBSD analysis. Textures in Mg were modified after alloying and extrusion.

Basal textures were found in HP-Mg, however, the texture direction was changed, and the texture intensity was enhanced in SPMg-xHo alloys (Fig. 1 (c)). The single-phased microstructures were also proved through the XRD patterns (Fig. 1 (d)), as only diffraction peaks from  $\alpha\text{-Mg}$  were detected both in as-cast and as-extruded alloys.

The single-phased microstructure in as-extruded alloys was further approved by performing TEM analysis, as shown in Fig. 2. Clean grain interiors and grain boundaries were found, and few small particles could be barely found at nanoscale. SAED patterns corresponding to the  $\alpha\text{-Mg}$  phase could be identified, with typical HR-TEM images showing the atomic arrangements (Fig. 2 (a)). Some tiny Ho-rich particles ( $<15 \text{nm}$ ) could be observed both inside the grains and at grain boundaries in SPMg-7.0Ho, and their numbers are still very limited (Fig. 2 (b)). Meanwhile, Zr-rich particles were rarely found. The bimodal grain microstructure was composed of alternately arranged DRXed zones and un-DRXed zones, with partially DRXed transitional zones between them. A high density of dislocations and sub-grain boundaries were found within the un-DRXed zones. However, only a few traces of dislocations could be found in the equiaxed grains adjacent to the un-DRXed zones. There was no appearance of dislocations in the fully recrystallized grains. The Ho element was found to be segregated at grain boundaries or sub-grain boundaries (both at DRXed zones and un-DRXed zones). All the constituent elements were uniformly distributed inside the grains, as proved by the EDS mapping (Fig. 2 (b)).

#### 3.2. Mechanical behaviors

Fig. 3 displays the mechanical properties of SPMg-xHo alloys compared to those of Mg and HP-Mg. The original stress-strain curves were included in Fig. S2. Mechanical properties of the SPMg-xHo series

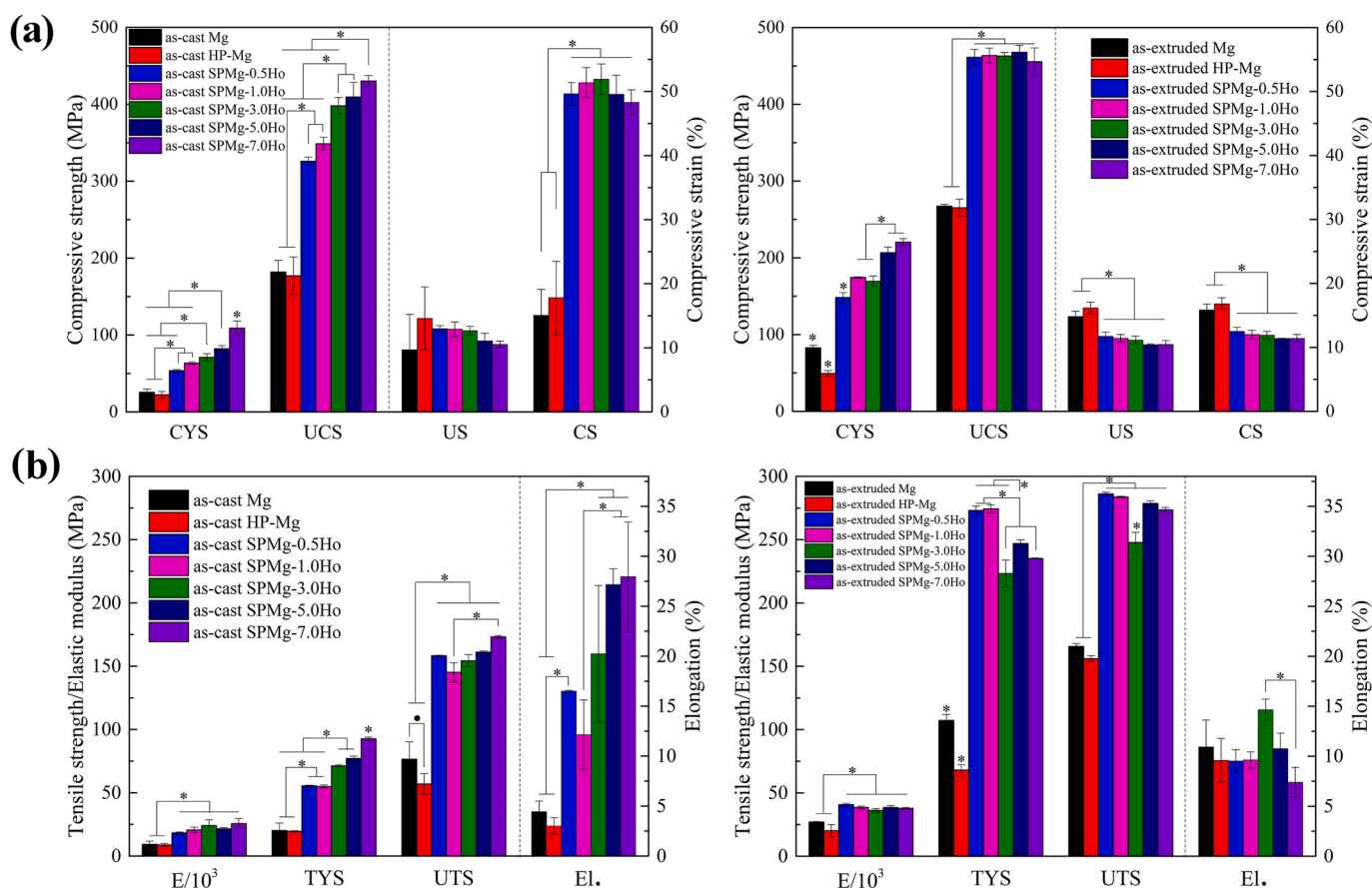


Fig. 3. (a) Mechanical properties of SPMg-xHo alloys derived from the compressive stress-strain curves; (b) mechanical properties of SPMg-xHo alloys derived from the tensile stress-strain curves, Mg and HP-Mg as controls.

alloys were significantly improved both in as-cast and as-extruded conditions. The extrusion processing could substantially improve or adjust the mechanical properties. All the mechanical parameters, except for tensile/compressive strains, were remarkably improved after extrusion. For the as-cast SPMg-xHo alloys, CYSS and TYSS gradually increased along with Ho addition, especially during compressive test. However, the influence of Ho content on CYSS and TYSS became inapparent after extrusion. Significant differences in tensile and compressive yield strengths between the two kinds of pure magnesium were found after extrusion, showing the significant effects of minor impurities on TYSS/CYSS of deformed Mg.

The CYSS, UCS, and CS of as-extruded Mg were 83 MPa, 267 MPa, and 16%, respectively. The CYSS and UCS were significantly improved to 148–220 MPa and 461–468 MPa for the SPMg-xHo alloys. However, the CS was decreased to 11–13%. The E, TYSS and UTS of as-extruded Mg were 27 GPa, 107 MPa and 166 MPa, respectively. They were improved to 36–41 GPa, 223–275 MPa and 247–287 MPa among the SPMg-xHo alloys, corresponding to the increase rates of 33–52%, 108–157% and 49–73%, respectively. The effect of alloying content on the mechanical properties is highly related to the processing state. The total alloying content in our single-phased alloys can be reduced after extrusion.

### 3.3. In-vitro degradation behaviors

#### 3.3.1. Electrochemical corrosion behaviors

Fig. 4 (a)–(c) shows the OCP, EIS and PDP results, and corresponding electrochemical parameters were listed in Table S2. When the sample was in contact with water, corrosion immediately occurred. Then, a degradation product layer gradually formed, and it would lead to the evolution of OCP curve. OCP values of all the experimental materials

increased with time, and they tended to be stabilized after immersion for 3000 s. The OCP curves of as-cast Mg, as-cast HP-Mg and as-cast SPMg-0.5Ho fluctuated frequently compared to the remaining ones, implying a poor equilibrium between the formation and dissolution/rupture of the degradation product layer. The addition of  $\geq 1.0$  wt% Ho helped to stabilize the dynamic equilibrium. A large fluctuation was still found on the OCP curve of Mg even after extrusion, although it owned the highest OCP value, as displayed in Fig. 4 (a).

For PDP curves, the anodic branch represents the dissolution of Mg while the cathodic polarization current reflects the severity of hydrogen evolution. The SPMg-xHo alloys exhibited lower cathodic current densities compared to that of the raw Mg, showing the inhibition effect of dissolved alloying elements in the alloy matrix. Cathodic current densities of as-cast SPMg-xHo alloys (except for the low Ho addition one, SPMg-0.5Ho) were close to that of as-cast HP-Mg. However, they were still higher than that of HP-Mg after extrusion, as shown in Fig. 4 (c). On the anodic branch, potential rise above the  $E_{corr}$  would cause increase in the anodic current. Under the same potential perturbation, the anodic current increase of as-extruded SPMg-xHo alloys was smaller than that of as-extruded Mg, suggesting inhibited anodic reaction. The  $i_{corr}$  values derived from the PDP curves could reflect the corrosion rates. After alloying with Ho and Zr, corrosion resistance of Mg could be significantly improved. The corrosion resistance of SPMg-xHo alloys was similar to that of HP-Mg. In addition, the extrusion processing also contributed to the corrosion resistance, as shown in Fig. 4 (e). It is well known that a larger loop in the EIS spectra (Nyquist plots) means better corrosion resistance [35]. The loops were enlarged after extrusion, and sizes of the loops were basically in accordance with their  $i_{corr}$  values (Fig. 4 (b)).

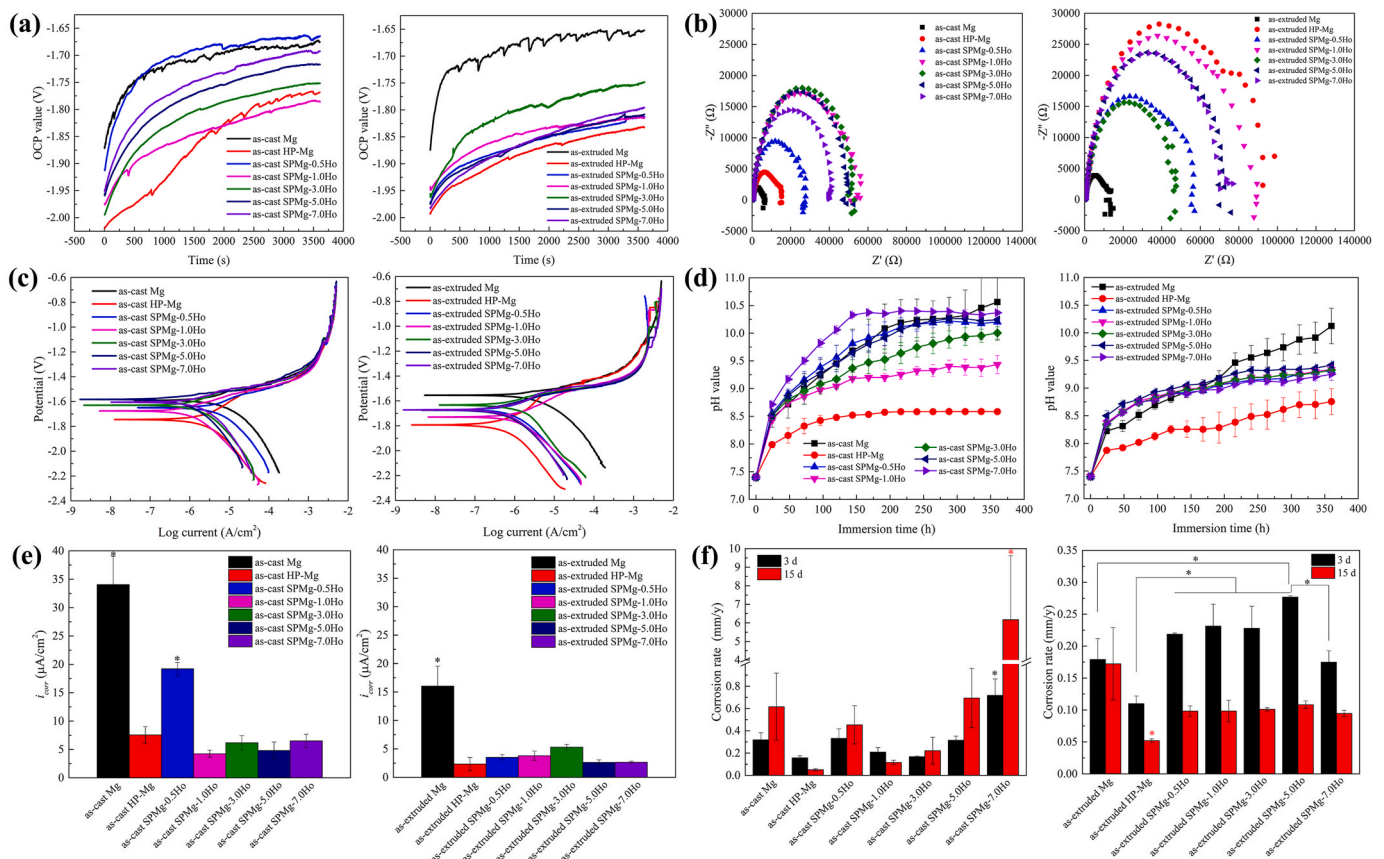


Fig. 4. Electrochemical corrosion results: (a) OCP curves, (b) EIS loops, (c) PDP results, and (e) corresponding  $i_{corr}$  derived from the PDP curves of SPMg-xHo alloys in Hank's solution, Mg and HP-Mg as control. Immersion corrosion results in Hank's solution: (d) pH evolution during immersion, and (f) corrosion rate calculated from weight loss.

3.3.2. Immersion corrosion behaviors

Fig. 4 (d) displays the pH evolution during a 15-day immersion. Generally, there was a rapid pH increase in the initial stage of immersion. Then, the pH value increased slowly and steadily, and finally reached at a relatively stable value. However, the pH value of Mg (as-cast/as-extruded) constantly increased, and did not stabilize even after immersion for 15 days due to intensified local corrosion. For the as-cast alloys, only as-cast SPMg-7.0Ho exhibited a more drastic pH increase and a higher pH value compared to those of raw Mg. The pH value and its increase rate were suppressed after extrusion. In addition, the pH value got to be stabilized (pH < 9.5) faster than their as-cast counterparts, as shown in Fig. 4 (d). There was no much difference in the pH evolution among different as-extruded SPMg-xHo alloys. HP-Mg exhibited the lowest pH value among all the experimental materials, implying its excellent corrosion resistance.

Fig. 4 (f) displays the corrosion rates calculated from weight losses. For as-cast SPMg-xHo alloys, proper alloying (Ho < 5 wt%) was favorable for the corrosion resistance. However, corrosion was apparently accelerated when Ho content reaching 7 wt%. As-cast Mg, as-cast SPMg-5.0Ho and as-cast SPMg-7.0Ho suffered from severely localized

corrosion (Fig. S3). This explained why their 15-day average corrosion rates were much higher than the 3-day results. Corrosion resistance of the experimental materials was more or less improved after extrusion, due to grain refinement and improved microstructural uniformity. Corrosion rates calculated from the two test methods (weight-loss and electrochemical test) were compared in Table S2. The differences in test methods and principles led to different values [36,37]. However, they all showed that proper alloying (full solid-solution) was favorable for the corrosion resistance of Mg, especially for the long-term corrosion resistance. From the perspective of corrosion, the Ho content in SPMg-xHo alloys could be minimized to 0.5 wt%.

Typical surface and cross-sectional morphologies of the as-extruded SPMg-xHo alloys are displayed in Fig. 5 (a). Since there was little difference among various SPMg-xHo alloys, only the corrosion morphologies of as-extruded SPMg-1.0Ho were shown. A degradation product (DP) layer was formed during immersion, and this layer became thicker along with immersion time. The corroded sample surface was composed of macroscopically uniform corrosion areas and non-uniform corrosion areas, as shown in Fig. 5 (a) and Fig. S3. Non-uniform corrosion areas (mildly localized corrosion areas) occurred on all the experimental

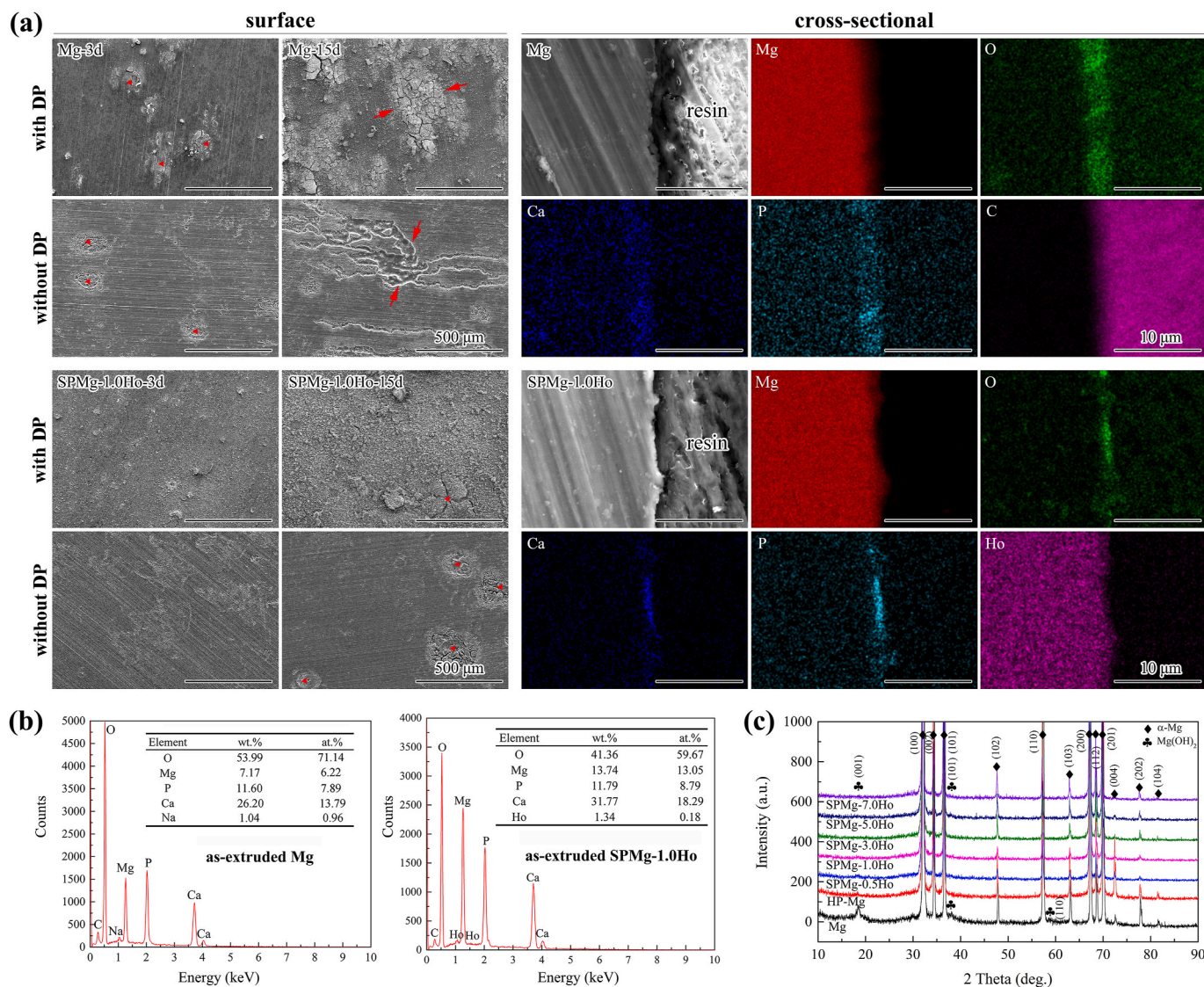
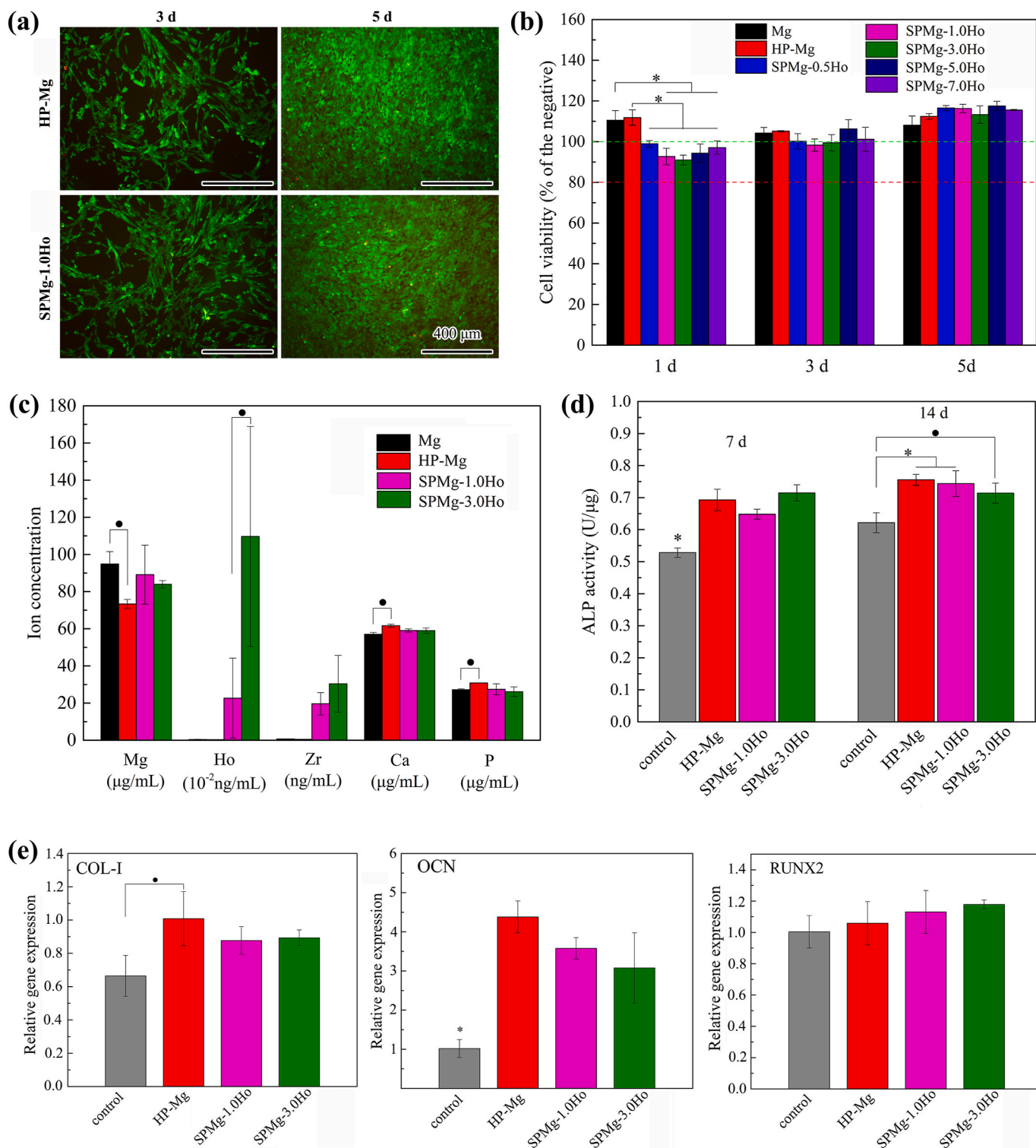


Fig. 5. (a) Typical corrosion morphologies (surface, both with degradation products and after removal of degradation products) and corresponding cross-sectional morphologies and EDS mapping of as-extruded SPMg-xHo alloys compared to those of as-extruded Mg (only as-extruded Mg and as-extruded SPMg-1.0Ho were shown. Red triangles marked the sites where non-uniform corrosion or mildly localized corrosion happened. Red arrows marked the sites where severely localized corrosion (filiform corrosion) happened.); (b) Chemical compositions on the corroded sample surface characterized by EDS; (c) XRD patterns of the corroded samples.

materials. However, severely localized corrosion (the filiform corrosion) was only observed on as-extruded Mg. Degradation products above the localized corrosion areas were incompact and with widespread cracks.

The actual morphology of the matrix was revealed after removing the degradation products. SPMg-xHo alloys and pure Mg all suffered from pitting corrosion on the microscopical level. Tiny pits could be found in

non-uniform corrosion areas, severely localized corrosion areas, and also in the macroscopically uniform corrosion areas. Severely localized corrosion was only found on as-extruded Mg. Surface and cross-sectional DES analysis revealed that the degradation products were mainly composed of Mg, O, Ca and P. A small amount of Ho was also detected on the corroded SPMg-xHo samples, as depicted in Fig. 5 (a) and (b). Fig. 5



**Fig. 6.** (a) LIVE/DEAD staining of the MC3T3-E1 cells after incubation with material extracts (green for living cells, red for dead cells, only the results of as-extruded HP-Mg and SPMg-1.0Ho were shown as they were similar for the remaining groups); (b) cell viability characterized through CCK-8 assay at 1, 3, 5 d; (c) ionic concentrations in typical extracts; (d) ALP activity at 7, 14 d; (e) expression of osteogenesis-related genes at 14 d. Only as-extruded SPMg-1.0Ho and SPMg-3.0Ho among the series alloys were evaluated for ALP activity and gene expression to reduce workload.

(c) displays the XRD patterns of all the experimental materials after immersion for 15 days. Diffraction peaks of  $Mg(OH)_2$  were detected on as-extruded Mg. However, the signals from  $Mg(OH)_2$  were quite weak of the remaining materials, implying that less degradation products existed.

### 3.4. In-vitro cell responses

#### 3.4.1. Cytotoxicity and ALP activity

Fig. 6 (a) and (b) show the MC3T3-E1 cell morphology and corresponding quantitative results of cell viability. Cells were well attached and spread in as-extruded SPMg-xHo extracts, and there were no

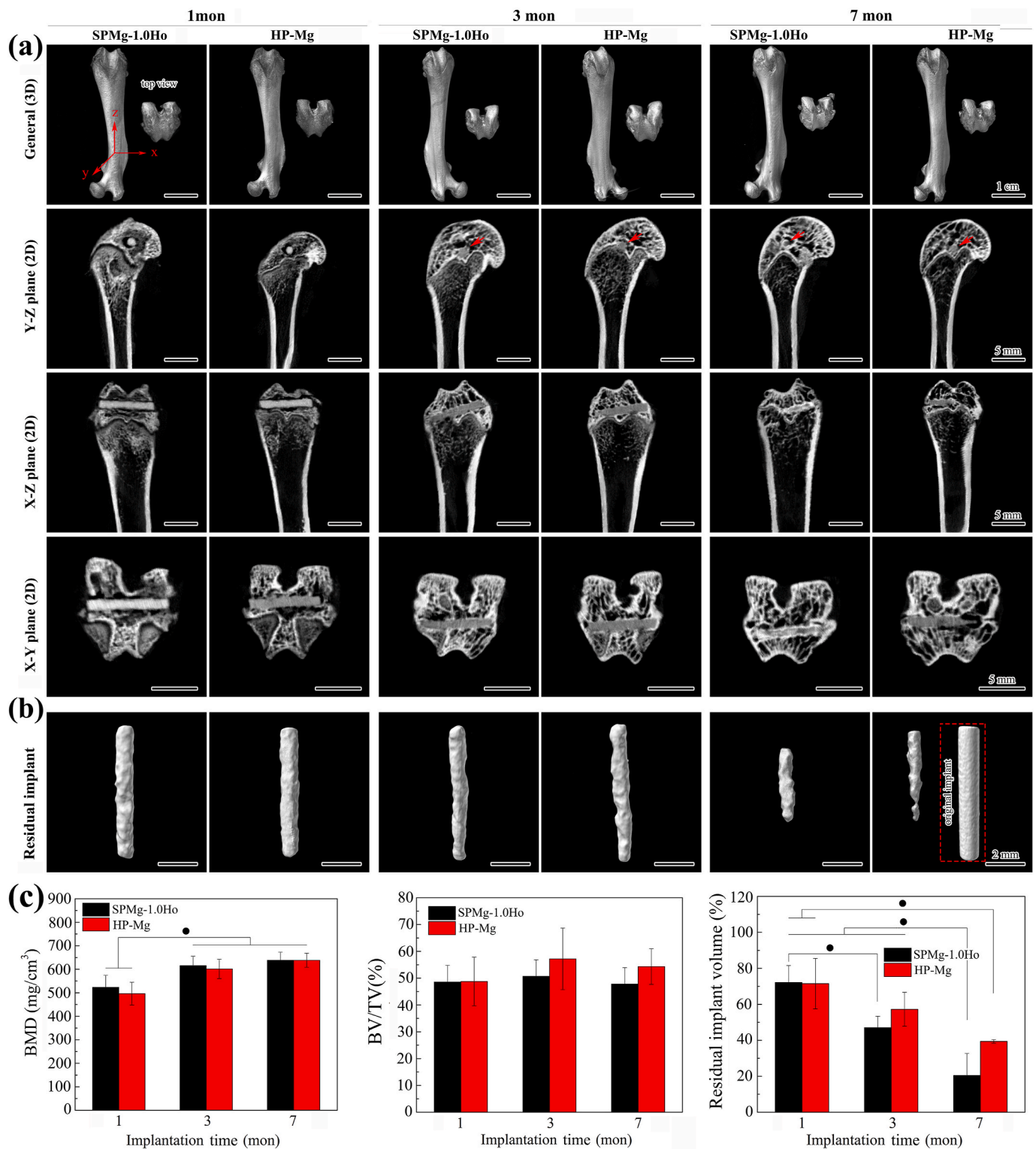


Fig. 7. (a) Micro-CT analysis (2D and 3D) of the rat femurs implanted with as-extruded SPMg-1.0Ho pins during a 7-month follow-up, with as-extruded HP-Mg pins as control (red arrows indicating the position of the implant); (b) 3D reconstruction of the residual implants, (c) BMD value around the implant, BV/TV value around the implant, and quantitative analysis of the residual implant volume.

distinguished differences compared to those of as-extruded Mg/HP-Mg. Cell viability in the SPMg-xHo extracts was lower than that of Mg/HP-Mg at the first day, however, it was improved at day 3 and day 5, showing gradual adaptation to the alloy extracts. There was no cytotoxicity of all the materials, since cell viability value was >90% during the whole culture period. Fig. 6 (c) displays the ionic concentrations in typical extracts. HP-Mg exhibited the lowest Mg concentration among all the experimental materials, showing its best corrosion resistance in cell culture medium. Significantly reduced Ca/P concentration of as-extruded Mg indicated that more Ca/P was deposited on Mg surface as it corroded more severe than others, corresponding to the results in Hank's solution. The Ho concentration in the extract increased with Ho addition in the alloy itself. In addition, Ho concentration was significantly lower than Zr concentration compared to their initial composition ratio, which meant Ho was more likely to incorporate into the degradation product layer. Increased ALP activity was observed for cells treated with Mg, HP-Mg and the SPMg-xHo extracts, compared to the blank control. However, there was no much difference among the experimental material groups, as shown in Fig. 6 (d).

#### 3.4.2. Expression of osteogenesis-related genes

Fig. 6 (e) shows the expression of three typical osteogenesis-related genes, including COL-1, OCN and RUNX2. The high expression of those genes means cells are prone to osteogenic differentiation, which is beneficial for bone formation. The HP-Mg and SPMg-xHo groups exhibited higher gene expression compared to that of the untreated group (control). However, significant difference was only found in OCN and in COL-1 (between HP-Mg and control). Gene expressions of the HP-Mg group and SPMg-xHo groups were similar. There was no significant difference between HP-Mg and SPMg-xHo alloys.

### 3.5. In-vivo performances

#### 3.5.1. Gross observation

One animal in the HP-Mg group died from abdominal infection (intraperitoneal injection induced) three days post-operation. Then, a new animal was supplemented. The remaining animals all survived, and no obvious signs of lameness and loss of appetite were observed. No deformity or neoplasm was found on the rat legs. No infection was found around the wounds or peri-implant tissues through autopsy and X-ray examination. There was no noticeable difference in the body sizes, main organ sizes and animal behaviors between those two groups. There was no abnormality on the appearance of the femoral condyle and the whole femur of both groups from gross observation.

#### 3.5.2. Implant degradation and bone-related parameters

Fig. 7 displays the micro-CT reconstructions (2D & 3D) and corresponding quantitative results, including BMD, BV/TV and residual implant volume. There was no noticeable abnormality on the morphology of the femoral condyle and the whole femur, as shown in the general 3D reconstruction in Fig. 7 (a). There were no signs of bone destruction or bone necrosis in both groups. Good osseointegration between the implant and surrounding cancellous bone was gradually achieved along with prolonged implantation time. Moderate bonding could be recognized in both groups after 1 month, as there were still some small gaps at some sites between the implant and adjacent bone tissues. The implant and surrounding bone tissues were well integrated after 3 months. Newly formed trabecular bone tissues were in direct contact with the implant. Furthermore, the good bonding could be maintained along with implant degradation.

Bone-related parameters, including BMD and BV/TV, were adopted to evaluate the bone conditions around the implant, as shown in Fig. 7 (c). BMD values were apparently improved at 3 months, and then remained stable afterwards, showing the maturation of rat bones at 3 months. BMD values of the two groups were quite similar at each time point. The two groups also exhibited comparable BV/TV values during

the whole implantation period. Continuous degradation of the implants (both SPMg-1.0Ho and HP-Mg) could also be observed. The surface of both implants became rougher after 1 month. Both implants kept intact at 3 months, even though they became much thinner. The implants were severely corroded after 7 months as some parts of the implant were fully corroded, as depicted in Fig. 7 (a) and (b). The implant volume losses of SPMg-1.0Ho and HP-Mg were similar at 1 month, and then the former exhibited a faster degradation rate. However, there was no statistical difference between those two groups, as depicted in Fig. 7 (c).

#### 3.5.3. Histological responses

Fig. 8 shows the histopathological results of bone tissues and main organs. No necrosis or excessive inflammatory response was found at local sites in the femurs. After 1 month, fibrous tissues surrounding the SPMg-1.0Ho implant or HP-Mg implant were found, as indicated by black arrows. Some osteoid tissues were torn away from their original position (surrounding the implant) during the section process in the SPMg-1.0Ho group. The fibrous tissues around the implants were disappeared after 3 months in both groups. Bone morphologies of the two groups were similar at 7 months. The morphologies of growth plates adjacent to the implant were displayed in Fig. 8 (b). The range/thickness of the growth plate significantly decreased at 7 months, showing the epiphyseal closure (femur won't grow after that). There were no observable differences on the growth plates between the two groups at each time point, and no difference in femoral length was observed. In addition, similar results were also found in the histological images of main organs between SPMg-1.0Ho and HP-Mg. Pathological images of main organs were quite similar, so only the 7-month results were displayed in Fig. 8 (c). Overall, SPMg-1.0Ho and HP-Mg exhibited similar local and systemic histological responses.

#### 3.5.4. Blood analysis

All the blood analysis results were listed in Table S3 in the form of mean value  $\pm$  standard deviation. Among the 35 testing items (including 19 for blood routine analysis, 12 for blood biochemistry analysis, and 4 for blood coagulation analysis), only those which showed obvious difference between SPMg-1.0Ho and HP-Mg, or those which exhibited apparent increase/decrease trend with time were displayed in Fig. S4. The WBC and LYMPH amounts of the two groups showed significant difference at 3 months, with SPMg-1.0Ho group exhibiting a lower value. However, no obvious difference was found after 7 months. The values of WBC and LYMPH decreased along with time, showing the postoperative inflammatory reaction gradually subsided. The items of PDW, MPV, P-LCR, TT and Fbs seemed to share a similar variation trend, i.e., those values gradually increased with time. Although some differences might be found between the two experimental groups (SPMg-1.0Ho and HP-Mg) at some time nodes, the relative differences were quite small compared to their normal fluctuation ranges. For the blood biochemistry items, AST value of the SPMg-1.0Ho group at 3 months was significantly higher than its counterpart (HP-Mg), but, they did not show statistical difference at 7 months. Even so, it still reminded us that overmuch alloying elements could possibly gain burden on liver and kidney. A little discrepancy in Urea and GLU contents did not mean much difference in clinical features, as food-intake, water-intake, and the pre-operation waiting time between those two groups could have influence on that. In general, blood testing items of SPMg-1.0Ho and HP-Mg were comparable, and SPMg-1.0Ho did not lead to anomalous changes in hemogram or occurrence of unexpected diseases.

#### 3.5.5. Tissue concentration of metal elements

Fig. 9 (a), (b) and (c) show the metal elements (Mg, Zr and Ho) in main organs, serums, urine and feces. Elemental concentrations in feces at 3 months were missing because of that the samples were unfortunately lost during ICP test. Zr concentrations of the HP-Mg group at 1 month were not tested. Except for urinary Mg, the Mg concentrations in main organs, serums and feces were generally stable, and there were no

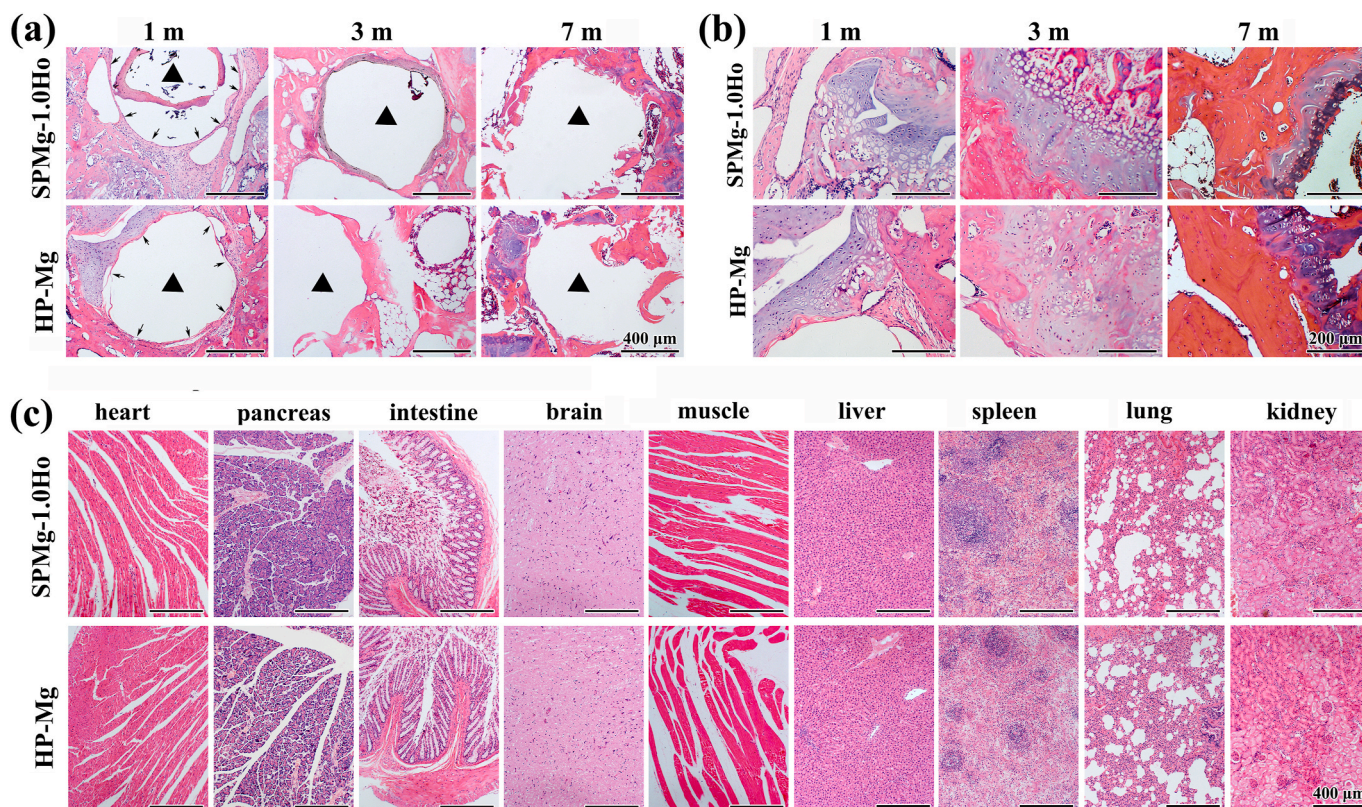


**Fig. 8.** (a) Histological analysis of the bone tissues surrounding the implants at different time intervals, with black triangles indicating the sites where the implant held before, and small arrows showing the fibrous tissues surrounding the implants at 1 month post-operation; (b) histological images of the adjacent growth plates at different time points; (c) histological comparison of main organs between SPMg-1.0Ho and HP-Mg.

major differences between the two groups. The Mg concentration in urine owned a large fluctuation range in both groups, which could range from single digits to several hundred  $\mu\text{g}/\text{mL}$  (4.34–753.5  $\mu\text{g}/\text{mL}$ ) without following any rules.

Zr element (trace element in human body) was detected in the HP-Mg group which did not introduce exogenous Zr by the material itself. The difference of Zr concentrations among various organs was inconspicuous in the HP-Mg group. Significantly higher Zr contents were detected in the main organs of the SPMg-1.0Ho group. The Zr content in brain tissues exhibited in a different manner compared to those of the remaining organs. The lowest Zr concentration was detected in brain at 1 month, then it fell into the same level of the HP-Mg group, probably due to the blood-brain barrier. Zr element tended to be accumulated in spleen, kidney and liver, as shown in Fig. 9 (b). However, Zr concentrations increased first (1–3 m), then gradually decreased after that (3–7 m). The Zr increase in heart (7 m) did not make much sense as Zr concentration (in heart) also increased with time in the HP-Mg group. The clearance of Zr in serum and urine was observed, as Zr concentrations in those fluids continuously decreased with prolonged implantation time. The Zr concentration in feces seemed to be stable judged by the limited results.

The *in-vivo* distribution and concentration change of Ho with implantation time were generally similar to that of Zr. However, no Ho was detected in the HP-Mg group (detection limit at 0.01 ng/g). Ho was more abundant in spleen, liver, lung and kidney, and the least Ho concentration was detected in brain. The difference between the maximum Ho concentration and the minimum Ho concentration could reach three orders of magnitude. The tissue concentration of Ho significantly increased from 1 month to 3 months, then, it dramatically decreased from 3 months to 7 months. Ho concentration at 7 months was even close to the result at 1 month. The Ho concentration in serum also followed the same rule, which was different from the variation of Zr in

serum. Ho content in urine decreased with prolonged implantation time, however, a constant Ho concentration was detected in animal feces. No detectable Ho was found in the feces of the animals in the HP-Mg group.

### 3.5.6. Characterization of the retrieved implants

Fig. 10 (a) displays the *in-vivo* corrosion morphologies of the retrieved SPMg-1.0Ho and HP-Mg implants, with enlarged images showing the typical surface details. Both implants kept intact in their shape before 3 months with implant diameter shrinking. Sample surface became rougher with prolonged implantation time. Some parts of the implants were completely degraded at 7 months. The implants were covered by a thick degradation product layer, and some superficial deposits on this layer were detached and adhered to the conducting resin. Cracks spread throughout this layer, probably due to the dehydration process.

The degradation product layer was composed of Mg, O, Ca, P, C and N for both SPMg-1.0Ho and HP-Mg, as shown in Fig. 10 (c). The high contents of C, O and N indicated that organic components might have been incorporated onto this layer. FTIR spectrum (Fig. 10 (b)) indicated the presence of possible functional groups, including  $\text{H}_2\text{O}$ ,  $\text{OH}^-$ ,  $\text{CO}_3^{2-}$ ,  $\text{PO}_4^{3-}$  and possible  $\text{H}_2\text{PO}_4^-$  [38]. Fig. 10 (d) shows the high resolution narrow XPS scanning results. The binding energy of P 2p at 133.5 eV was related to  $\text{PO}_4^{3-}$  or  $\text{HPO}_4^{2-}$ , as also proved in FTIR results. The existence of  $\text{Ca}_5(\text{PO}_4)_3(\text{OH})$  (HA) was confirmed as indicated by the P 2p peak at 133.5 eV and Ca 2p peak at 347.3 eV [39,40]. The Ca 2p peaks (350.9 eV for Ca 2p<sub>1/2</sub>, 347.3 eV for Ca 2p<sub>3/2</sub>) and P 2p peak (133.5 eV) confirmed calcium phosphate formed at the sample surface [41]. The single Mg 2p peak at 50.3 eV and one O 1s peak at 532.8 eV suggested the possible existence of MgO, or the mixture of  $\text{MgO}/\text{Mg}(\text{OH})_2$  [42,43]. All those degradation products were compatible with bone tissues. The N 1s spectra revealed two components, centered at 399.8 eV and 402.4 eV, which could correspond to organic components in human body [44].

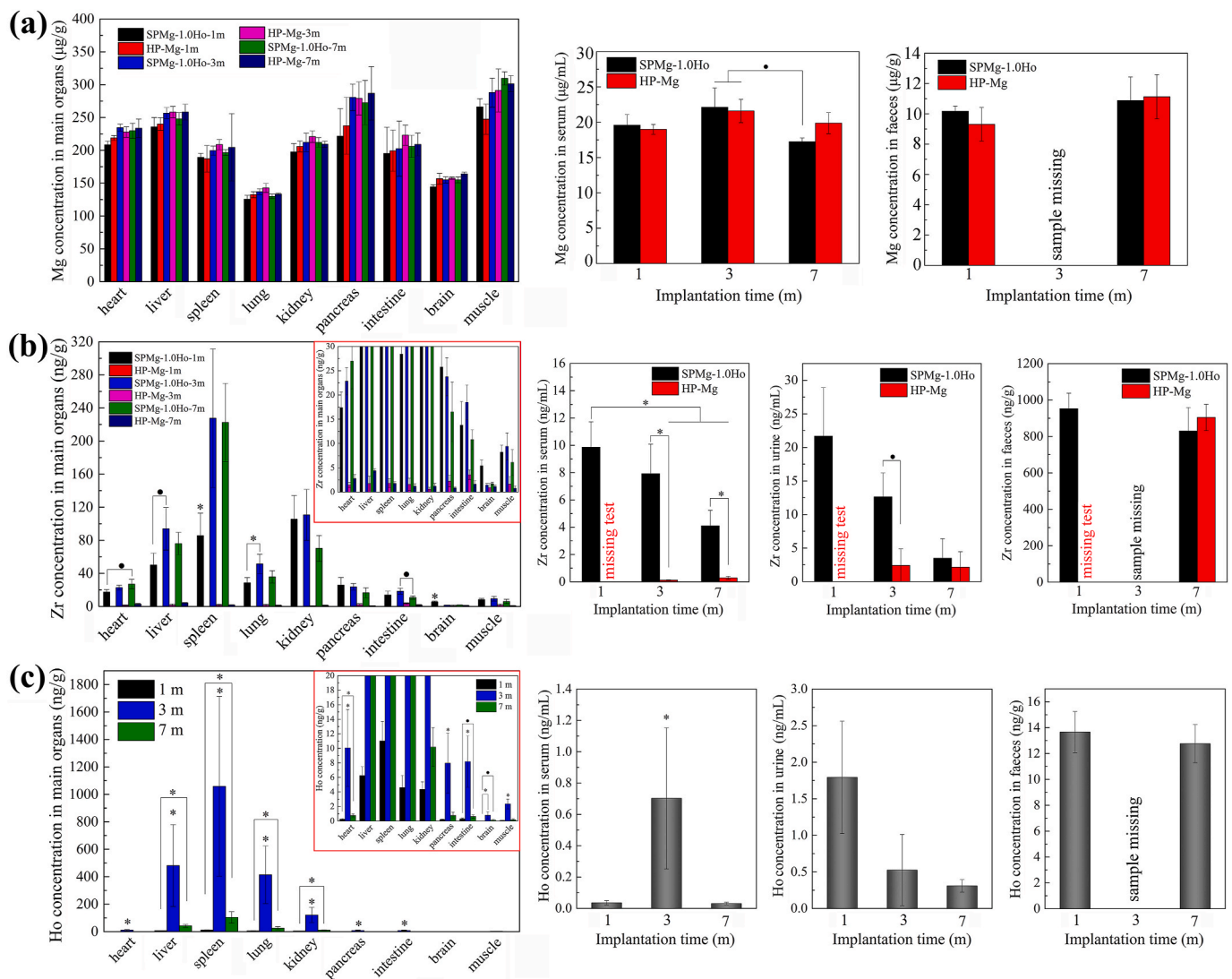


**Fig. 9.** (a) Mg concentrations in main organs, serums and feces (from left to right); (b) Zr concentrations in main organs, serums, urea and feces (from left to right), with magnification of the local area as insert; (c) Ho concentrations in main organs, serums, urea and feces (from left to right, the local area is magnified and displayed as insert).

Most of those degradation products were in amorphous state examined with SAED under HR-TEM, and a small amount of crystalline substances were unstable under electron beam in TEM.

## 4. Discussion

### 4.1. General effects of REEs on Mg properties

Significant effects of REEs in Mg could be concluded in the following paragraphs, considering the perspectives of metallurgy, microstructure, mechanical properties and corrosion behaviors. The specific roles of Ho on those aspects in our single-phased alloys will be detailedly discussed. The influence of metal elements on biological safety will be separately discussed in the next section.

#### 4.1.1. REEs on metallurgy

REEs play an important role in bulk purification by reducing hydrogen, oxygen and sulfur in the melt, and also by removing impurities (such as Fe, Cu, Ni and Co) during smelting (the so-called “scavenger effect”) [2,45]. This effect has been proved in this series alloys, as the contents of Ni, Cu, Co, Mn and Al were reduced with Ho addition, meanwhile, Fe and Si contents kept at the same level of raw Mg (Table 2

and Fig. S5). The impurity contents were below their tolerance limits, above which corrosion would be dramatically accelerated (Fig. S5) [11]. The total impurity contents did not constantly decrease with Ho addition since those impurities also existed in the Mg-30Ho master alloy.

#### 4.1.2. REEs on microstructure and mechanical properties

REEs addition in Mg can normally weaken the strong basal texture, enhance non-basal slip activities, and improve the deformability [46, 47]. The grain refinement effect of REEs can contribute to strength and ductility simultaneously [48]. RE atoms which dissolve into the crystal lattice will lead to lattice distortion, and cause the so-called solid-solution strengthening. Undissolved RE atoms can form intermetallics with Mg or other alloying elements, leading to the precipitation strengthening or second phase strengthening [46,49,50]. Specific microstructures, such as long period stacking ordered (LPSO) structure, pre-twinning structures, bimodal grain structure, etc., can be achieved in RE containing magnesium alloys, and contribute to the mechanical properties [51].

Bimodal grain structures composed of DRXed regions with fine grains and un-DRXed regions (coarse grains) with abundant sub-grain microstructures were achieved in our SPMg-xHo alloys, which were not reported in binary Mg–Zr alloys. Lately, bimodal-grained structures

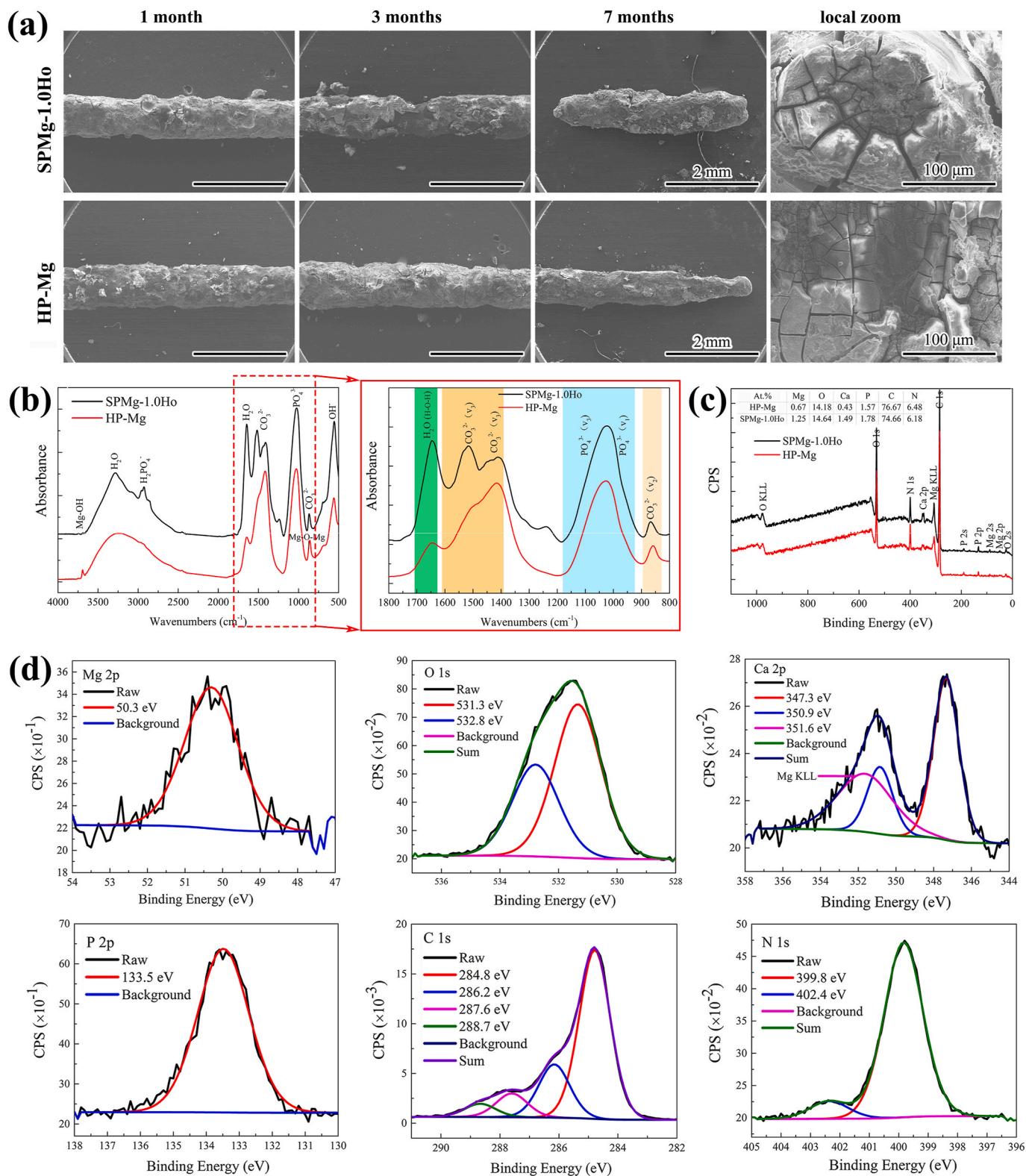


**Fig. 10.** (a) Surface morphologies of the retrieved SPMg-1.0Ho and HP-Mg implants after implantation for different periods, with typical enlarged images showing the surface details; (b) FTIR spectra of the retrieved SPMg-1.0Ho and HP-Mg implants, with amplification of specific area at the range of 800–1800 cm<sup>-1</sup>; (c) XPS spectra of the retrieved implants at 3 months, with quantification results of the constituent elements as insert; (d) high-resolution narrow XPS scanning results of the retrieved implant.

consisting of both ultrafine grains (UFGs)/fine grains (FGs) and coarse grains (CGs) have been proposed as an efficient strategy in achieving a superior combination of strength and ductility [52]. Incomplete and heterogeneous dynamic recrystallization resulted in the microstructures composed of alternately DRXed and un-DRXed regions. Alloying elements could efficiently refine the microstructure and prevent grain growth during dynamic recrystallization. Ho addition can effectively prevent grain growth during dynamic recrystallization during extrusion (Fig. 1 (b)). The average grain size of as-extruded SPMg-7.0Ho is  $1.8 \pm 1.3 \mu\text{m}$ , much finer than that of as-extruded SPMg-1.0Ho ( $2.4 \pm 1.9 \mu\text{m}$ ) with lower Ho addition (Fig. S1 (a)). The improved mechanical properties were mainly derived from grain refinement and solid solution strengthening. The bimodal grain structures containing textures, twisted grain boundaries, sub-grains and sub-grain structures (residual dislocations and Ho enriched sub-grain boundaries) formed during extrusion further contributed to the mechanical properties (Fig. 1, Fig. S1) [51]. Mechanical properties of as-extruded SPMg-xHo alloys did not differ too much in the Ho addition range. So, Ho content in the alloys could be minimized to 0.5 wt% or even lower with those microstructural characteristics. With a good combination of strength and ductility, mechanical properties of our SPMg-xHo alloys were comparable to those of current Mg-based products (CE marked) [53,54]. The total 7 wt% REEs in commercial MAGNEZIX® or Magmaris® (WE43) might be replaced by the single Ho addition (0.5 wt%), showing that less RE is doing more. Microstructures and mechanical properties of the SPMg-xHo alloys were reconfirmed after 3 years, and they were stable, which ensured those alloys own a long useful life or shelf life.

#### 4.1.3. REEs on corrosion behaviors

The “scavenger effect” of REEs in Mg can reduce the detrimental effects of impurities to Mg corrosion [45]. RE oxides or hydroxides

generated during corrosion might incorporate into the degradation product layer, and contribute to the film completeness and compactness, thus improve corrosion resistance [55]. The corrosion potentials of REEs are close to that of Mg, which leads to a reduction in the potential difference between the intermetallic compounds and  $\alpha$ -Mg matrix. This will play an important role in reducing galvanic corrosion [45].

For our SPMg-xHo series alloys, the scavenger effect has been proved, which helped to lower the adverse effects of impurities. Without second phases, galvanic corrosion between different phases could be basically avoided. Ho was reported to own a slightly higher standard electrode potential than Mg [12], however, OCP values of SPMg-xHo alloys were lower than that of the raw Mg, but still higher than that of HP-Mg. It also implied the significant effects of impurities on OCP value. Ho was found to be incorporated into the degradation product layer (Fig. 5 (a)–(b) and Fig. 6 (c)), which was believed to retard the kinetic process of Mg corrosion.

All the experimental materials were suffered from microscopic pitting corrosion, since pitting is the first step of Mg corrosion (basic corrosion mode of Mg). With corrosion proceeding, some non-uniform corrosion areas developed (dark areas in the macroscopic images shown in Fig. 11 (a) and pockmarks shown in Fig. 11 (c)). Newly-formed local corrosion areas continued to appear while the pre-existing ones gradually developed in transverse and longitudinal directions with prolonged immersion time. In general, concentrated development towards the longitudinal direction (in depth direction) would lead to aggravated corrosion, which should be avoided for Mg-based biomaterials. The non-uniform corrosion areas could be distinguished and quantified in ImageJ 1.43u software, as shown in Fig. 11 (a) and (b). At day 3, HP-Mg owned the highest area fraction of non-uniform corrosion, while SPMg-xHo series alloys exhibited the minimal localized corrosion. At day 15, the non-uniform corrosion areas on HP-Mg were

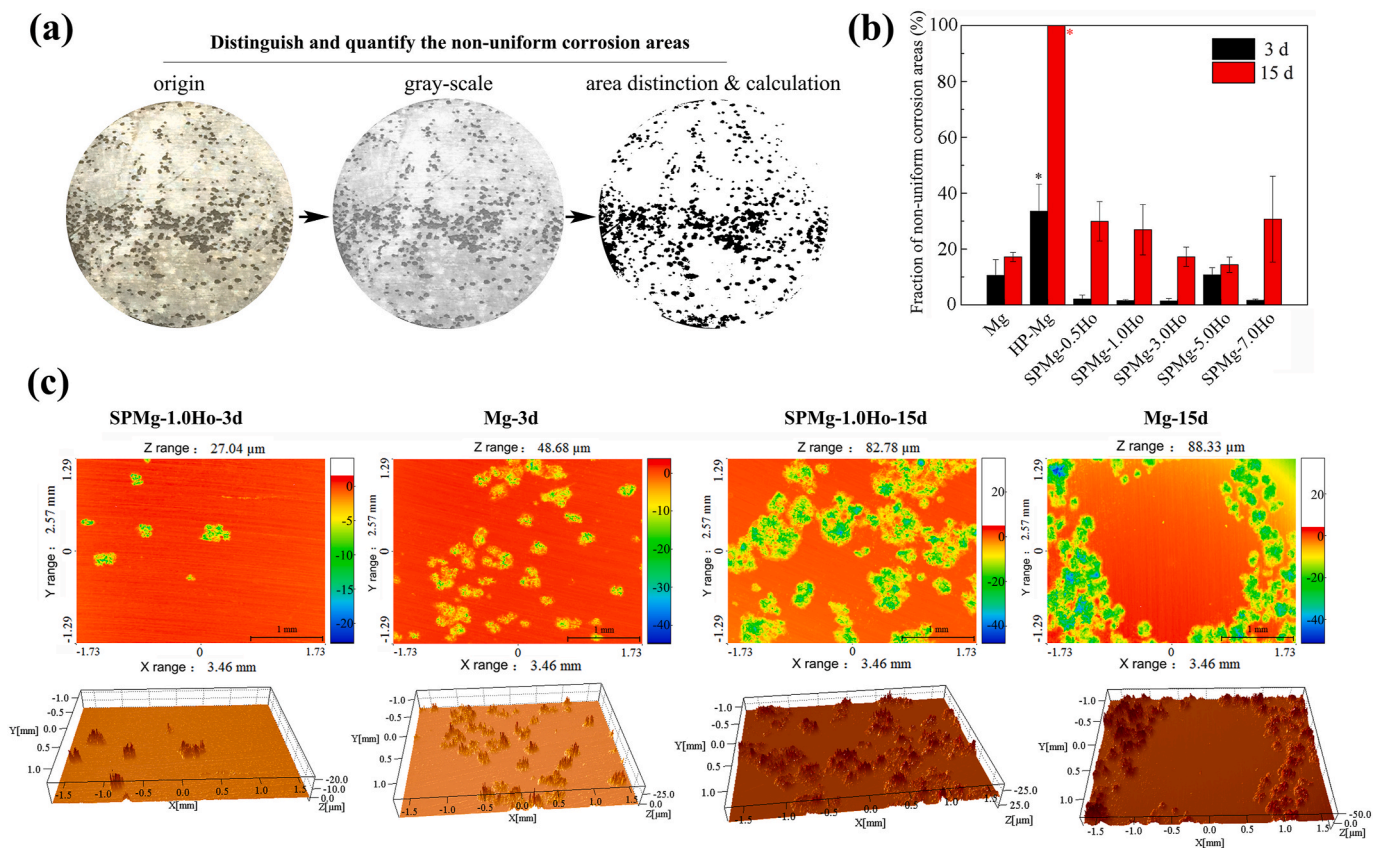


**Fig. 11.** (a) Schematic steps showing how to distinguish and quantify the non-uniform corrosion areas on as-extruded samples (after removing the degradation products) in ImageJ software; (b) quantitative results of the non-uniform corrosion areas on corroded samples; (c) surface profiles (2D and 3D) of the corroded samples characterized through a surface profile measurement system (Talysurf PGI 1230), which is based on the white-light interference measuring technique.

fully interconnected (100% coverage). However, it exhibited the minimum corrosion rate because of the smallest corrosion depth. The fractions of non-uniform corrosion areas on SPMg-xHo alloys were similar to that of Mg, but the former exhibited a lower corrosion depth. Ho addition inhibited the corrosion development in depth due to its beneficial effects that mentioned before.

#### 4.2. Multi-scale biological safety of the SPMg-xHo alloys

Once implanted *in vivo*, the bioactive Mg-based implant and the host cells/tissues participate in local chemical/physiological reactions at the interface [56]. Elements in the alloy will be released along with degradation in the form of metal ions. Meanwhile, a part of them may be incorporated into the degradation products layer at the implant surface. Soluble ions or solid degradation products might be absorbed, metabolized, and transferred by adjacent (local) cells/tissues [57,58]. Metal elements which entered into blood would be transferred to remote organs/tissues, and made possible impacts. So, a systemic observation on those affected organs/tissues is also needed. Proper host responses without possible local & systemic toxicity are crucial for implantable materials and devices [59–60]. The biological safety of SPMg-Ho alloys would be considered on multi-levels, including cellular biocompatibility, tissue biocompatibility and whole-body (systemic) biocompatibility.

##### 4.2.1. Cellular and molecular levels

Biocompatibility or toxicity of a certain element is dose-dependent, which also relies on its existence form (free ion, chelate or compound) and intake pathway. Mg is a major element in human body with a total content of  $\geq 10$  g. However, Ho and Zr belong to the trace elements (with unknown functions in human body), and their body contents only account for  $< 1$  mg, 10000 times lower than Mg [58]. The 50% inhibitory concentrations ( $IC_{50}$ ) of Mg to various cells are much higher than the alloying elements (Ho, Zr). Zr is normally found in human tissues, and  $IC_{50}$  of Zr to MC3T3 cells was reported to be 258.2  $\mu\text{g}/\text{mL}$  ( $2.83 \times 10^{-3}$  mol/L) [61]. In our previous study, A Mg-10Ho alloy with a fast degradation rate did not show cytotoxicity to MC3T3 cells [17]. So, the low ionic concentrations ( $< 100$   $\mu\text{g}/\text{mL}$  Mg,  $< 1.2$  ng/mL Ho and  $< 40$  ng/mL Zr) in alloy extracts did not lead to adverse cell responses. Cell viability, cell morphology, ALP concentration and bone-related gene expression were all comparable to those of HP-Mg, showing good *in vitro* biocompatibility at the cellular and genetic levels.

##### 4.2.2. Tissue and systemic levels

The body has a strong ability to balance Mg. Excessive Mg can be excreted efficiently through the urinary system.  $LD_{50}$  of  $\text{MgCl}_2$  obtained via oral supplement in mouse was reported to be as high as 5000 mg/kg [58]. Recommended daily allowance of Mg is 320–400 mg [40]. It demonstrated that no difference or a slight increase (but still in normal range) of the Mg concentration could be found in different tissues or serum after Mg implantation in published literatures and also in this study [62]. Mg released from the SPMg-1.0Ho alloy would not induce adverse effects. Zr is regarded as a nontoxic trace element with unknown function in human body, and its total body content is  $\sim 1$  mg. It is unusually found in bioinert (nonbiodegradable) implant, which exhibit excellent biocompatibility and corrosion resistance [63]. A small amount of Zr is also added in two clinically-proven Mg-based bone screws, which implies that limited Zr in Mg-based implant is tolerable by the body [24].

On the contrary, there is limited understanding of the biological impact of REEs. REEs can be detected in human tissues, as the intake source could be from food and water. The recommended maximum allowance of REEs in food is 4.2 mg/day [64]. In addition, some REEs have been investigated as additives for fertilizer and animal feeds [65]. Even so, Ho element is poorly studied [64]. Ho compounds are known to stimulate the metabolism of the human body, but their biological effects

are still controversial [66]. Trivalent chloride of Ho below 5  $\mu\text{g}/\text{mL}$  did not show cytotoxicity to human vascular smooth muscle cells [67].  $LD_{50}$  for Ho chloride obtained via intraperitoneal supplement in mouse was reported to be 560 mg/kg [58]. A SPMg-1.0Ho based bone screw weighing 100 mg (approximate size of  $\Phi 3.0 \times 10$  mm) contains only 1 mg Ho, which is far below that toxicity limit. No abnormality was found on various tissues (local bone tissue and main organs) between SPMg-1.0Ho and HP-Mg. New bone could directly lay down onto the implant and grew along its surface, showing good bone biocompatibility and osseointegration. Mg, Zr and Ho in animal blood did not lead to abnormal changes in blood parameters, showing the good hemocompatibility. Similar hepatic and renal function indexes between the two groups meant that Ho and Zr could be well tolerated by local and remote organs/tissues. Overall, the SPMg-1.0Ho alloy exhibited good *in-vivo* biocompatibility without local or systemic toxicity.

##### 4.2.3. Metabolism of metal elements

The metabolic mechanism of degradation products from Mg based implants is very different from those from oral-administration or intraperitoneal supplement. Although the metabolic mechanism of Mg implants has received attention, studies rarely reveal the metabolic pathway and efficiency of alloying elements, which may be substantially different from those of Mg element [68]. Constituent elements in the SPMg-1.0Ho alloy were minor Ho and Zr with balanced Mg. Mg is well-tolerated by the body, displaying exceedingly low toxicity and rapid excretion through the urinary system. On the contrary, some REEs were reported to be accumulated in main organs (such as liver, kidney, lung, etc.) after taking a large dose or a long-term low dose, which can lead to pathological changes or even metabolic disorders [64]. The biological transport pathways appear to differ with atomic radius, with the lighter lanthanides predominantly fecally excreted, and so processed through the liver, versus the heavier lanthanides, which are disposed of through the urinary tract [69]. Regarding this matter, the element concentration and distribution in various tissues and body fluids were carefully checked at different time points. Metallic elements (Ho and Zr) derived from the implant were transferred into different organs through the blood circulation. Those elements could be gradually eliminated from the body through the urinary system and digestive system. Gradual clearance of those heavy metals was observed in our SPMg-1.0Ho alloy, and this reduced the metabolic pressure of organs and tissues.

Even though the alloying elements would not likely to be accumulated in animal body, REEs are not naturally common in biochemical processes and, as such, the body has limited specialized mechanisms for dealing with these elements. For meeting the performance requirements, REEs in biomedical magnesium alloys should be minimized to avoid possible biological hazards. The concept and technical approach of single-phased alloys seem to be feasible.

#### 4.3. Further proof of the concept

The pure  $\alpha$ -Mg single-phased microstructure enables high purity magnesium with excellent biocompatibility and corrosion resistance. However, due to limited strengthening mechanisms, high purity magnesium exhibits poor mechanical properties. In traditional multi-phased Mg-RE alloys, mechanical properties can be improved through precipitation of a large amount of RE-containing phases or compounds. To achieve sufficient improvements in mechanical properties and corrosion resistance, plenty of REEs are usually needed, which also brings possible safety concerns. In this study, the single-phased Mg-Ho based alloys integrate the advantages of high purity magnesium and multi-phased RE-containing alloys, and at the same time avoid their shortcomings. Could this rule be extended to other high-solubility REEs?

RE solubility, potential difference and atomic radius difference (vs. Mg) should be considered when design a single-phased Mg-RE alloy, as shown in Fig. 12. Except for Sc, the remaining REEs will go through a eutectic reaction with Mg during cooling of the melt. A fast cooling rate

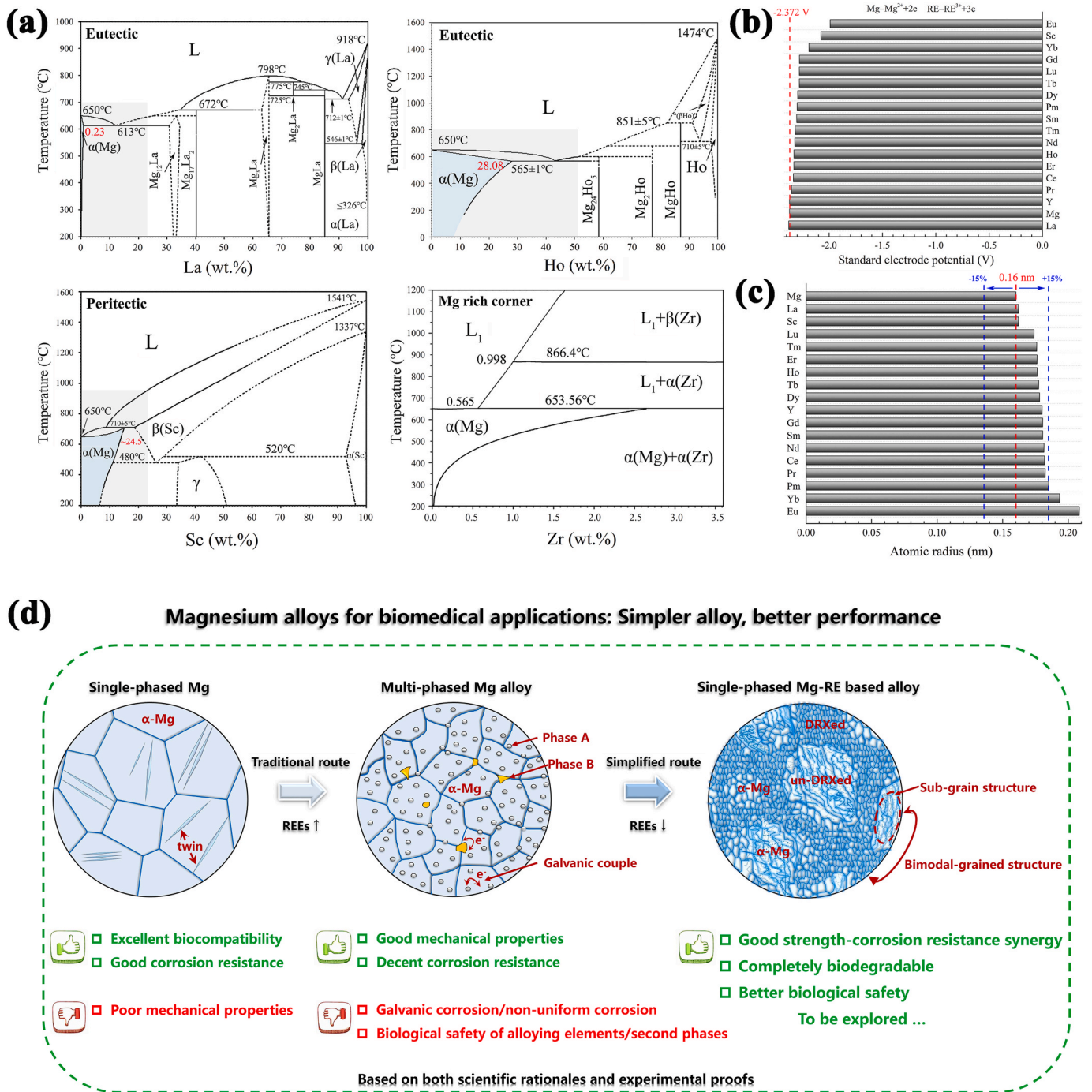


Fig. 12. (a) Typical phase diagrams of binary Mg-RE alloys with limited-solubility or high-solubility REEs. Mg-rich corner of the Mg-Zr system is also included (b) potential difference (vs. Mg); and (c) atomic radius difference (vs. Mg) of REEs; (d) the “simpler alloy, better performance” concept and technical approach in this study.

is good for solid-solution of REEs. The limited-solubility REEs will tend to combine with Mg to form intermetallic compounds, and to form the coarse eutectic microstructures. The smaller the solid solubility, the more difficult it is to obtain a single-phased microstructure. The maximum solubility of Zr in Mg is reported to be 2.65 wt % [70]. Minor Zr addition, which does not combine with REEs during solidification, will ensure a single-phased microstructure. To minimize the potential difference between the second phases and the Mg matrix is an efficient way to reduce the galvanic corrosion in multi-phased Mg-RE alloys (Fig. 12 (b)). However, is this applicable to single-phased Mg-RE alloys still need to be explored. The atomic size within ±15% of the atomic size

of Mg is favorable for the formation of a solid-solution with Mg (Fig. 12 (c)) [10]. All in all, the main concept and technical approach of this study were generally summarized in Fig. 12 (d).

Two more high-solubility REEs, i.e. Er and Lu (maximum solubility >30 wt%, with considerable solubility even at room temperature) were chosen, and single-phased microstructures (with bimodal-grained characteristics) were successfully achieved in those alloys though the most common smelting, casting and extrusion procedures. Mechanical properties and corrosion resistance of as-obtained SPMg-xEr and SPMg-xLu alloys were significant improved compared to those of the raw Mg. All the single-phased series alloys showed good biocompatibility to

MC3T3-E1 cells. In general, the newly developed SPMg-xEr and SPMg-xLu series alloys exhibited comparable performances to the SPMg-xHo series alloys (Fig. 13), just as we expected. Unexpected precipitation of Lu-rich particles in SPMg-7.0Lu led to galvanic corrosion, and impaired the corrosion resistance (insert in Fig. 13 (c)). It implies that a pure single-phased microstructure is the basis for good corrosion resistance. Based on all those theoretical rationales and experimental evidences, we believe that the design theory of single-phased Mg-RE alloys can be applied or refereed during R&D process of other biodegradable metals.

#### 4.4. Future work

Simpler alloys have already been proposed for engineering applications to improve sustainability, and it has been proved that the high performance of alloys can be maintained with compositional “plainification” [71]. In the case of Mg-RE alloys for biomedical applications, simpler alloys (both in alloying compositions and constituent phases) mean better biological safety. Low alloying or ultra-low alloying (<0.1 wt%) is highly expected in biodegradable metals. High-purity or ultrahigh-purity raw materials are recommended to fabricate those alloys. RE addition in single-phased magnesium alloys might be minimized though playing with defects in metals, such as controlling of twins, solute clusters, and grain boundary characteristics, etc. [72]. Single-phased alloys seem to be suitable for implant applications with small size, such as stent and suture applications, so, research on those aspects could be expected.

## 5. Conclusions

In this work, we are trying to introduce the concept of developing single-phased magnesium alloys with typical high solubility REEs for biomedical applications, and prove it with sufficient experimental data. Fine single-phased Mg-RE model alloys with bimodal microstructures were successfully fabricated. The microstructural characteristics endow good corrosion resistance with a uniform corrosion mode, and provide sufficient strengthening effects. Mechanical properties of our single-phased alloys are comparable to those of clinically applied Mg-based products. The typical SPMg-1.0Ho alloy exhibited similar *in vitro* and *in vivo* performances compared with a high purity magnesium, showing the good corrosion resistance and biocompatibility. In addition, metallic elements in this alloy were gradually excreted through the urinary system and digestive system. Compared to the commercial WE43-based implant applications, significantly reduced RE addition in our single-phased alloys is hopefully beneficial to the biocompatibility, and to lower the potential risks of biological hazards. Other biodegradable metals with single-phased microstructures are expected to be explored.

#### CRediT authorship contribution statement

**Dong Bian:** Conceptualization, Methodology, Formal analysis, Investigation, Writing – original draft. **Xiao Chu:** Methodology, Investigation, Writing – review & editing. **Jin Xiao:** Investigation, Supervision. **Zhipei Tong:** Investigation, Validation. **He Huang:** Investigation. **Qinggong Jia:** Investigation. **Jianing Liu:** Investigation. **Wenting Li:** Investigation. **Hui Yu:** Formal analysis, Investigation. **Yue He:** Investigation. **Limin Ma:** Investigation. **Xiaolan Wang:** Investigation,

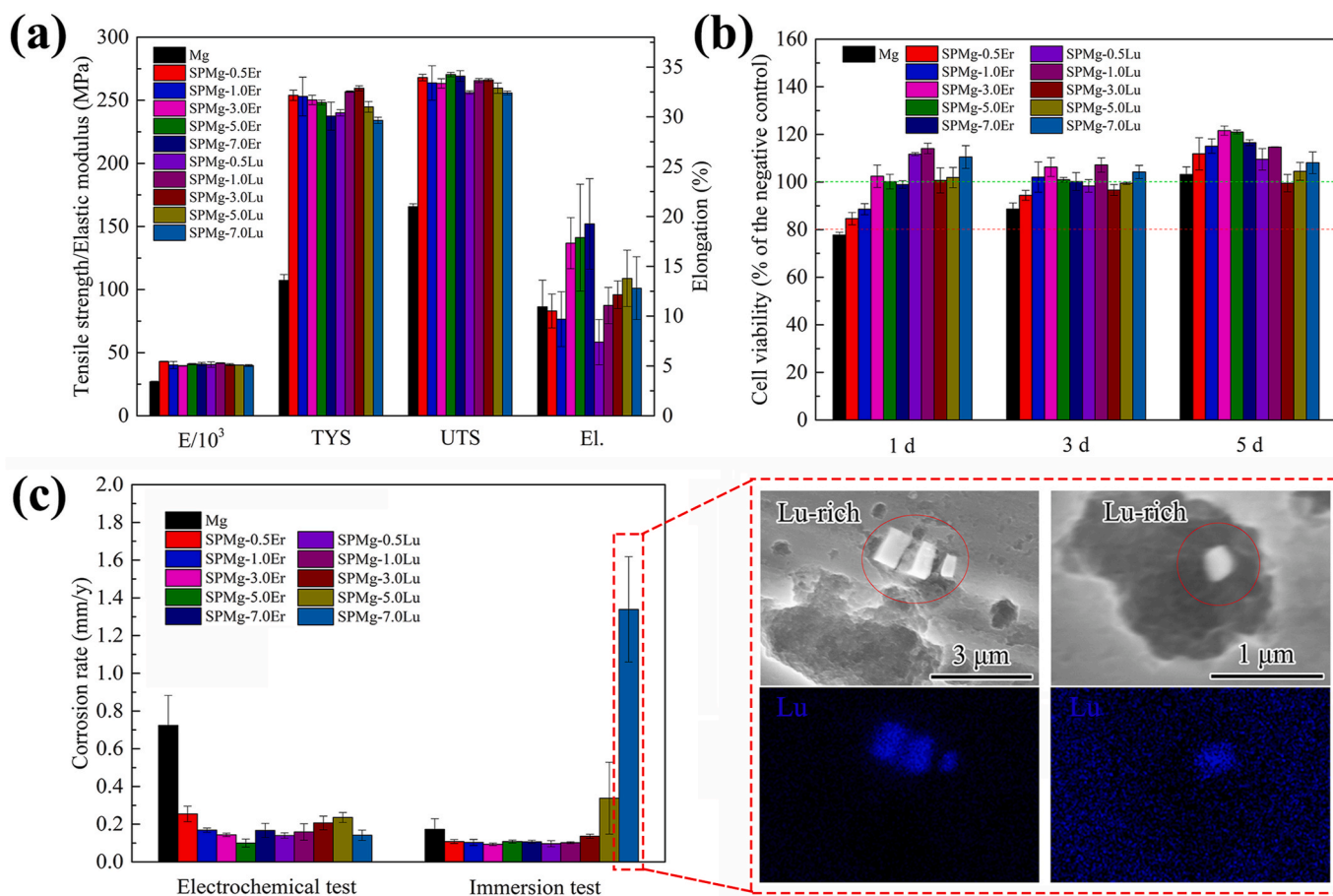


**Fig. 13.** (a) Mechanical properties, (b) cell viability, and (c) corrosion rates of two more single-phased Mg-RE series alloys, i.e., as-extruded SPMg-xEr and SPMg-xLu ( $x = 0.5, 1.0, 3.0, 5.0, 7.0$ ) alloys. The inset shows the Lu-rich second phase particles and related galvanic corrosion.

Visualization. **Mei Li:** Investigation. **Tao Yang:** Methodology, Investigation. **Wenhan Huang:** Investigation, Visualization. **Chi Zhang:** Visualization. **Mengyu Yao:** Methodology, Investigation. **Yu Zhang:** Supervision, Funding acquisition. **Zhigang Xu:** Conceptualization, Resources, Supervision. **Yufeng Zheng:** Conceptualization, Resources, Writing – review & editing, Supervision, Project administration, Funding acquisition.

### Declaration of competing interest

The authors declare that they have no known competing financial interests or personal relationships that could have appeared to influence the work reported in this paper.

### Acknowledgements

This work was supported by the National Key R&D Program of China (Grant No. 2021YFC2400700), the National Natural Science Foundation of China (Grant No. 52101283), the Science and Technology Planning Project of Guangzhou (Grant No. 202201011454), the NSFC Incubation Program of GDPH (Grant No. KY012021165), and the High-level Hospital Construction Project (Grant No. KJ012019520).

### Appendix A. Supplementary data

Supplementary data to this article can be found online at <https://doi.org/10.1016/j.bioactmat.2022.09.018>.

### References

- I.S. Hirschhorn, Recent applications of the rare earth metals in nonferrous metallurgy, *J. Miner. Met. Mater. Soc.* 22 (10) (1970) 40–43, <https://doi.org/10.1007/BF03355666>.
- A. Biesiekierski, Y. Li, C. Wen, The application of the rare earths to magnesium and titanium metallurgy in Australia, *Adv. Mater.* 32 (2020), 1901715, <https://doi.org/10.1002/adma.201901715>.
- J. Xie, J. Zhang, Z. You, S. Liu, K. Guan, R. Wu, J. Wang, J. Feng, Towards developing Mg alloys with simultaneously improved strength and corrosion resistance via RE alloying, *J. Magnes. Alloy.* 9 (1) (2021) 41–56, <https://doi.org/10.1016/j.jma.2020.08.016>.
- D. Liu, D. Yang, X. Li, S. Hu, Mechanical properties, corrosion resistance and biocompatibilities of degradable Mg-RE alloys: a review, *J. Mater. Res. Technol.* 8 (1) (2019) 1538–1549, <https://doi.org/10.1016/j.jmrt.2018.08.003>.
- P. Sekar, N. S. V. Desai, Recent progress in in vivo studies and clinical applications of magnesium based biodegradable implants – a review, *J. Magnes. Alloy.* 9 (4) (2021) 1147–1163, <https://doi.org/10.1016/j.jma.2020.11.001>.
- J.-L. Wang, J.-K. Xu, C. Hopkins, D.H.-K. Chow, L. Qin, Biodegradable magnesium-based implants in orthopedics—a general review and perspectives, *Adv. Sci.* 7 (8) (2020), 1902443, <https://doi.org/10.1002/advs.201902443>.
- H.-S. Han, S. Loffredo, I. Jun, J. Edwards, Y.-C. Kim, H.-K. Seok, F. Witte, D. Mantovani, S. Glyn-Jones, Current status and outlook on the clinical translation of biodegradable metals, *Mater. Today* 23 (2019) 57–71, <https://doi.org/10.1016/j.mattod.2018.05.018>.
- A. Hideo-Kajita, H.M. Garcia-Garcia, P. Kolm, V. Azizi, Y. Ozaki, K. Dan, H. Ince, S. Kische, A. Abizaid, R. Töelg, P.A. Lemos, N.M. Van Mieghem, S. Verheye, C. von Birgelen, E.H. Christiansen, W. Wijns, T. Lefèvre, S. Windecker, R. Waksman, M. Haude, Comparison of clinical outcomes between Magmaris and Orsiro drug eluting stent at 12 months: pooled patient level analysis from BIOSOLVE II-III and BIOFLOW II trials, *Int. J. Cardiol.* 300 (2020) 60–65, <https://doi.org/10.1016/j.ijcard.2019.11.003>.
- V. Zepf, *Rare Earth Elements*, Springer, Berlin, 2013.
- Y. Chen, Z. Xu, C. Smith, J. Sankar, Recent advances on the development of magnesium alloys for biodegradable implants, *Acta Biomater.* 10 (11) (2014) 4561–4573, <https://doi.org/10.1016/j.actbio.2014.07.005>.
- Y. Zheng, *Magnesium Alloys as Degradable Biomaterials*, CRC Press, 2015.
- W.M. Haynes, *CRC Handbook of Chemistry and Physics*, 93rd Edition, CRC Press, 2012.
- G. Song, A. Atrens, Understanding magnesium corrosion—a framework for improved alloy performance, *Adv. Eng. Mater.* 5 (12) (2003) 837–858, <https://doi.org/10.1002/adem.200310405>.
- M. Cihova, P. Schmutz, R. Schäublin, J.F. Löffler, Biocorrosion zoomed in: evidence for dealloying of nanometric intermetallic particles in magnesium alloys, *Adv. Mater.* 31 (42) (2019), 1903080, <https://doi.org/10.1002/adma.201903080>.
- M. Esmaily, J.E. Svensson, S. Fajardo, N. Birbilis, G.S. Frankel, S. Virtanen, R. Arrabal, S. Thomas, L.G. Johansson, Fundamentals and advances in magnesium alloy corrosion, *Prog. Mater. Sci.* 89 (2017) 92–193, <https://doi.org/10.1016/j.pmatsci.2017.04.011>.
- M. Deng, L. Wang, D. Höche, S.V. Lamaka, C. Wang, D. Snihirova, Y. Jin, Y. Zhang, M.L. Zheludkevich, Approaching “stainless magnesium” by Ca micro-alloying, *Mater. Horiz.* 8 (2021) 589–596, <https://doi.org/10.1039/D0MH01380C>.
- J. Liu, D. Bian, Y. Zheng, X. Chu, Y. Lin, M. Wang, Z. Lin, M. Li, Y. Zhang, S. Guan, Comparative in vitro study on binary Mg-RE (Sc, Y, La, Ce, Pr, Nd, Sm, Eu, Gd, Tb, Dy, Ho, Er, Tm, Yb and Lu) alloy systems, *Acta Biomater.* 102 (2020) 508–528, <https://doi.org/10.1016/j.actbio.2019.11.013>.
- J. Xu, X. Chen, Y. Xu, Y. Du, C. Yan, Ultrathin 2D rare-earth nanomaterials: compositions, syntheses, and applications, *Adv. Mater.* 32 (3) (2020), 1806461, <https://doi.org/10.1002/adma.201806461>.
- O.D. Jungesblut, M. Moritz, A.S. Spiro, R. Stuecker, M. Rupperecht, Fixation of unstable osteochondritis dissecans lesions and displaced osteochondral fragments using new biodegradable magnesium pins in adolescents, *Cartilage* 13 (Suppl. 1) (2021) 302S–310S, <https://doi.org/10.1177/1947603520942943>.
- Y.C. Lee, A.K. Dahle, D.H. Stjohn, The role of solute in grain refinement of magnesium, *Metall. Mater. Trans. A* 31 (11) (2000) 2895–2906, <https://doi.org/10.1007/BF028330349>.
- D.H. Stjohn, M. Qian, M.A. Easton, P. Cao, Z. Hildebrand, Grain refinement of magnesium alloys, *Metall. Mater. Trans. A* 36 (7) (2005) 1669–1679, <https://doi.org/10.1007/s11661-005-0030-6>.
- S. Ragamouni, J.M. Kumar, D. Mushahary, H. Nemani, G. Pande, Histological analysis of cells and matrix mineralization of new bone tissue induced in rabbit femur bones by Mg–Zr based biodegradable implants, *Acta Histochem.* 115 (7) (2013) 748–756, <https://doi.org/10.1016/j.acthis.2013.03.004>.
- Y. Li, C. Wen, D. Mushahary, R. Sravanthi, N. Harishankar, G. Pande, P. Hodgson, Mg–Zr–Sr alloys as biodegradable implant materials, *Acta Biomater.* 8 (8) (2012) 3177–3188, <https://doi.org/10.1016/j.actbio.2012.04.028>.
- K. Xie, L. Wang, Y. Guo, S. Zhao, Y. Yang, D. Dong, W. Ding, K. Dai, W. Gong, G. Yuan, Y. Hao, Effectiveness and safety of biodegradable Mg–Nd–Zn–Zr alloy screws for the treatment of medial malleolar fractures, *J. Orthop. Transl.* 27 (2021) 96–100, <https://doi.org/10.1016/j.jot.2020.11.007>.
- ASTM E8/E8M-16a, Standard Test Methods for Tension Testing of Metallic Materials, ASTM International, West Conshohocken, PA, 2016. [www.astm.org](http://www.astm.org).
- ASTM E9-19, Standard Test Methods of Compression Testing of Metallic Materials at Room Temperature, ASTM International, West Conshohocken, PA, 2019. [www.astm.org](http://www.astm.org).
- ASTM E112-13, Standard Test Methods for Determining Average Grain Size, ASTM International, West Conshohocken, PA, 2013. [www.astm.org](http://www.astm.org).
- D. Mei, S.V. Lamaka, X. Lu, M.L. Zheludkevich, Selecting medium for corrosion testing of bioabsorbable magnesium and other metals – a critical review, *Corrosion Sci.* 171 (2020), 108722, <https://doi.org/10.1016/j.corsci.2020.108722>.
- ASTM-G102-89, Standard Practice for Calculation of Corrosion Rates and Related Information from Electrochemical Measurements. Annual Book of ASTM Standards Philadelphia, American Society for Testing and Materials, Pennsylvania USA, 1999.
- ASTM F3268-18a, Standard Guide for in Vitro Degradation Testing of Absorbable Metals, ASTM International, West Conshohocken, PA, 2018. [www.astm.org](http://www.astm.org).
- ASTM G31-72, Standard Practice for Laboratory Immersion Corrosion Testing of Metals, ASTM International, West Conshohocken, PA, 2004. [www.astm.org](http://www.astm.org).
- ASTM G1-03(2017)e1, Standard Practice for Preparing, Cleaning, and Evaluating Corrosion Test Specimens, ASTM International, West Conshohocken, PA, 2017. [www.astm.org](http://www.astm.org).
- Z. Shi, M. Liu, A. Atrens, Measurement of the corrosion rate of magnesium alloys using Tafel extrapolation, *Corrosion Sci.* 52 (2) (2010) 579–588, <https://doi.org/10.1016/j.corsci.2009.10.016>.
- ISO 10993-5:2009(E), *Biological Evaluation of Medical Devices —Part 5: Tests for in Vitro Cytotoxicity*, International Organization for Standardization, 2009.
- Z. Li, G.-L. Song, S. Song, Effect of bicarbonate on biodegradation behaviour of pure magnesium in a simulated body fluid, *Electrochim. Acta* 115 (2014) 56–65, <https://doi.org/10.1016/j.electacta.2013.10.131>.
- G. Song, A. Atrens, D.S. John, X. Wu, J. Nairn, The anodic dissolution of magnesium in chloride and sulphate solutions, *Corrosion Sci.* 39 (10–11) (1997) 1981–2004, [https://doi.org/10.1016/S0010-938X\(97\)00090-5](https://doi.org/10.1016/S0010-938X(97)00090-5).
- N.T. Kirkland, N. Birbilis, M.P. Staiger, Assessing the corrosion of biodegradable magnesium implants: a critical review of current methodologies and their limitations, *Acta Biomater.* 8 (3) (2012) 925–936, <https://doi.org/10.1016/j.actbio.2011.11.014>.
- P.K. Bowen, J. Drelich, J. Goldman, Magnesium in the murine artery: probing the products of corrosion, *Acta Biomater.* 10 (3) (2014) 1475–1483, <https://doi.org/10.1016/j.actbio.2013.11.021>.
- H. Tang, Y. Gao, Preparation and characterization of hydroxyapatite containing coating on AZ31 magnesium alloy by micro-arc oxidation, *J. Alloys Compd.* 688 (2016) 699–708, <https://doi.org/10.1016/j.jallcom.2016.07.079>.
- D. Bian, W. Zhou, J. Deng, Y. Liu, W. Li, X. Chu, P. Xiu, H. Cai, Y. Kou, B. Jiang, Y. Zheng, Development of magnesium-based biodegradable metals with dietary trace element germanium as orthopaedic implant applications, *Acta Biomater.* 64 (2017) 421–436, <https://doi.org/10.1016/j.actbio.2017.10.004>.
- T. Fu, J.T. Fan, Y.G. Shen, J.M. Sun, Hydrothermal calcification of alkali treated titanium in CaHPO<sub>4</sub> solution, *Mater. Chem. Phys.* 189 (2017) 105–110, <https://doi.org/10.1016/j.matchemphys.2016.12.056>.
- S. Ardizzone, C.L. Bianchi, M. Fadoni, B. Vercelli, Magnesium salts and oxide: an XPS overview, *Appl. Surf. Sci.* 119 (3) (1997) 253–259, [https://doi.org/10.1016/S0169-4332\(97\)00180-3](https://doi.org/10.1016/S0169-4332(97)00180-3).
- L. Prince, M.A. Rousseau, X. Noirfalsie, L. Dangreau, L.B. Coelho, M.G. Olivier, Inhibitive effect of sodium carbonate on corrosion of AZ31 magnesium alloy in NaCl solution, *Corrosion Sci.* 179 (2021), 109131, <https://doi.org/10.1016/j.corsci.2020.109131>.

- [44] W. Yan, Y.-J. Lian, Z.-Y. Zhang, M.-Q. Zeng, Z.-Q. Zhang, Z.-Z. Yin, L.-Y. Cui, R.-C. Zeng, In vitro degradation of pure magnesium—the synergetic influences of glucose and albumin, *Bioact. Mater.* 5 (2) (2020) 318–333, <https://doi.org/10.1016/j.bioactmat.2020.02.015>.
- [45] G.L. Song, *Corrosion Prevention of Magnesium Alloys*, Woodhead Publishing Limited, 2013.
- [46] A. Imandoust, C.D. Barrett, T. Al-Samman, K.A. Inal, H. El Kadiri, A review on the effect of rare-earth elements on texture evolution during processing of magnesium alloys, *J. Mater. Sci.* 52 (1) (2017) 1–29, <https://doi.org/10.1007/s10853-016-0371-0>.
- [47] J. Wu, L. Jin, J. Dong, F. Wang, S. Dong, The texture and its optimization in magnesium alloy, *J. Mater. Sci. Technol.* 42 (2020) 175–189, <https://doi.org/10.1016/j.jmst.2019.10.010>.
- [48] K. Lu, Stabilizing nanostructures in metals using grain and twin boundary architectures, *Nat. Rev. Mater.* 1 (5) (2016), 16019, <https://doi.org/10.1038/natrevmats.2016.19>.
- [49] Y. Li, C. Yang, X. Zeng, P. Jin, D. Qiu, W. Ding, Microstructure evolution and mechanical properties of magnesium alloys containing long period stacking ordered phase, *Mater. Char.* 141 (2018) 286–295, <https://doi.org/10.1016/j.matchar.2018.04.044>.
- [50] A.C. Lund, C.A. Schuh, *Mechanical properties: strengthening mechanisms in metals*, in: F. Bassani, G.L. Liedl, P. Wyder (Eds.), *Encyclopedia of Condensed Matter Physics*, Elsevier, Oxford, 2005, pp. 306–311.
- [51] Z.-Z. Jin, M. Zha, S.-Q. Wang, S.-C. Wang, C. Wang, H.-L. Jia, H.-Y. Wang, Alloying design and microstructural control strategies towards developing Mg alloys with enhanced ductility, *J. Magnes. Alloy.* 10 (5) (2022) 1191–1206, <https://doi.org/10.1016/j.jma.2022.04.002>.
- [52] E. Ma, T. Zhu, Towards strength–ductility synergy through the design of heterogeneous nanostructures in metals, *Mater. Today* 20 (6) (2017) 323–331, <https://doi.org/10.1016/j.mattod.2017.02.003>.
- [53] H. Windhagen, K. Radtke, A. Weizbauer, J. Diekmann, Y. Noll, U. Kreimeyer, R. Schavan, C. Stukenborg-Colsman, H. Waizy, Biodegradable magnesium-based screw clinically equivalent to titanium screw in hallux valgus surgery: short term results of the first prospective, randomized, controlled clinical pilot study, *Biomed. Eng. Online* 12 (1) (2013) 62, <https://doi.org/10.1186/1475-925X-12-62>.
- [54] J.W. Lee, H.S. Han, K.J. Han, J. Park, H. Jeon, M.R. Ok, H.K. Seok, J.P. Ahn, K. E. Lee, D.H. Lee, Long-term clinical study and multiscale analysis of in vivo biodegradation mechanism of Mg alloy, *Proc. Natl. Acad. Sci. USA* 113 (3) (2016) 716–721, <https://doi.org/10.1073/pnas.151823811>.
- [55] W. Liu, F. Cao, L. Chang, Z. Zhang, J. Zhang, Effect of rare earth element Ce and La on corrosion behavior of AM60 magnesium alloy, *Corrosion Sci.* 51 (6) (2009) 1334–1343, <https://doi.org/10.1016/j.corsci.2009.03.018>.
- [56] Y. Li, Y. Xiao, C. Liu, The horizon of materiobiology: a perspective on material-guided cell behaviors and tissue engineering, *Chem. Rev.* 117 (5) (2017) 4376–4421, <https://doi.org/10.1021/acs.chemrev.6b00654>.
- [57] Y.F. Zheng, X.N. Gu, F. Witte, Biodegradable metals, *Math. Sci. Eng. R* 77 (2014) 1–34, <https://doi.org/10.1016/j.msere.2014.01.001>.
- [58] Y. Liu, Y. Zheng, X.-H. Chen, J.-A. Yang, H. Pan, D. Chen, L. Wang, J. Zhang, D. Zhu, S. Wu, K.W.K. Yeung, R.-C. Zeng, Y. Han, S. Guan, Fundamental theory of biodegradable metals—definition, criteria, and design, *Adv. Funct. Mater.* 29 (18) (2019), 1805402, <https://doi.org/10.1002/adfm.201805402>.
- [59] ISO/TS 20721-2020, *Implants for Surgery — General Guidelines and Requirements for Assessment of Absorbable Metallic Implants*, International Organization for Standardization, 2020.
- [60] ISO 10993-11:2017, *Biological Evaluation of Medical Devices — Part 11: Tests for Systemic Toxicity*, International Organization for Standardization, 2017.
- [61] A. Yamamoto, R. Honma, M. Sumita, Cytotoxicity evaluation of 43 metal salts using murine fibroblasts and osteoblastic cells, *J. Biomed. Mater. Res.* 39 (2) (1998) 331–340, [https://doi.org/10.1002/\(SICI\)1097-4636\(199802\)39:2<331::AID-JBM22>3.0.CO;2-E](https://doi.org/10.1002/(SICI)1097-4636(199802)39:2<331::AID-JBM22>3.0.CO;2-E).
- [62] P. Holweg, V. Herber, M. Ormig, G. Hohenberger, N. Donohue, P. Puchwein, A. Leithner, F. Seibert, A lean bioabsorbable magnesium-zinc-calcium alloy ZX00 used for operative treatment of medial malleolus fractures, *Bone Joint Res* 9 (8) (2020) 477–483, <https://doi.org/10.1302/2046-3758.98.BJR-2020-0017.R2>.
- [63] D. Chopra, A. Jayasree, T. Guo, K. Gulati, S. Ivanovski, Advancing dental implants: bioactive and therapeutic modifications of zirconia, *Bioact. Mater.* 13 (2022) 161–178, <https://doi.org/10.1016/j.bioactmat.2021.10.010>.
- [64] W. Weng, A. Biesiekierski, Y. Li, M. Dargusch, C. Wen, A review of the physiological impact of rare earth elements and their uses in biomedical Mg alloys, *Acta Biomater.* 130 (2021) 80–97, <https://doi.org/10.1016/j.actbio.2021.06.004>.
- [65] M. Adeel, J.Y. Lee, M. Zain, M. Rizwan, A. Nawab, M.A. Ahmad, M. Shafiq, H. Yi, G. Jilani, R. Javed, R. Horton, Y. Rui, D.C.W. Tsang, B. Xing, Cryptic footprints of rare earth elements on natural resources and living organisms, *Environ. Int.* 127 (2019) 785–800, <https://doi.org/10.1016/j.envint.2019.03.022>.
- [66] S.-H. Shin, H.-O. Kim, K.-T. Rim, Worker safety in the rare earth elements recycling process from the review of toxicity and issues, *Saf. Health Work* 10 (4) (2019) 409–419, <https://doi.org/10.1016/j.shaw.2019.08.005>.
- [67] A. Drynda, N. Deinet, N. Braun, M. Peuster, Rare earth metals used in biodegradable magnesium-based stents do not interfere with proliferation of smooth muscle cells but do induce the upregulation of inflammatory genes, *J. Biomed. Mater. Res., Part A* 91 (2) (2009) 360–369, <https://doi.org/10.1002/jbm.a.32235>.
- [68] X. Lin, Sajjilafu, X. Wu, K. Wu, J. Chen, L. Tan, F. Witte, H. Yang, D. Mantovani, H. Zhou, C. Liang, Q. Yang, K. Yang, L. Yang, Biodegradable Mg-based alloys: biological implications and restorative opportunities, *Int. Mater. Rev.* (2022), <https://doi.org/10.1080/09506608.2022.2079367>. Ahead-of-print.
- [69] C.H. Evans, *Biochemistry of the Lanthanides*, Springer, Boston, 1990.
- [70] H. Okamoto, Mg-Zr (Magnesium-Zirconium), *J. Phase Equilibria Diffus.* 28 (3) (2007) 305–306, <https://doi.org/10.1007/s11669-007-9060-7>.
- [71] X. Li, K. Lu, Improving sustainability with simpler alloys, *Science* 364 (6442) (2019) 733–734, <https://doi.org/10.1126/science.aaw9905>.
- [72] X. Li, K. Lu, Playing with defects in metals, *Nat. Mater.* 16 (7) (2017) 700–701, <https://doi.org/10.1038/nmat4929>.